# Relativistic Reflection

## -

## A Generalization of the Lamp Post Model

**Masterarbeit aus der Physik**


vorgelegt von

**Stefan Lickleder**

25. November 2019

Astronomisches Institut Dr. Karl-Remeis Sternwarte
Friedrich-Alexander-Universität Erlangen-Nürnberg
Department Physik




Betreuer: Prof. Dr. Jörn Wilms

# Relativistic Reflection

A Generalization of the Lamp Post Model

**Stefan Lickleder**

## Abstract

Several observations of black holes clearly show broadened reflection features in the received energy spectrum. These features are explained by the relativistic reflection of high-energetic X-ray photons at the innermost regions of the black hole's accretion disk. In these regions, special- and general relativistic effects have noticeable influence on the photon's trajectories. Therefore, various parameters, such as the black hole spin parameter or the location of the irradiating X-ray source are encoded in the relativistic smearing of the reflection features. There exist models, that predict the observed spectra by assuming an X-ray source on the axis of symmetry of the black hole system, illuminating the accretion disk. These models however are not applicable for potential X-ray sources deviating from the axis of symmetry or extended sources that do not lie completely on said axis. The main goal of this thesis is to provide a physical approach to model the relativistic reflection for a general photon source in Kerr-spacetime.
Although models using the lamp post geometry, i.e., irradiation by an X-ray source on the axis of symmetry of the black hole system, can explain many of the observed features, a treatment of general photon sources is needed to investigate whether the lamp post geometry is unique in explaining these features and quantifying the conformity of the chosen source geometry to observed spectra. The treatment of a general photon source is realized in this thesis, based on the *YNOGK*-code for null-like trajectories in Kerr-spacetime provided by Yang & Wang (2013). The results of the model are shown to agree with previous works on the lamp post geometry and on general point sources. Additionally, results for the illumination of the accretion disk by ring sources of varying height and radius, centered around the axis of symmetry are shown and the dependency on the source parameters is discussed. The angular dependence of the irradiation by a point source is investigated as well and the possibility of constructing any general photon source of finite extent by superposition of multiple point sources is discussed. Finally, the modelling of the reflection features by concatenation of the presented method with existing reflection models such as the *relxill* model is outlined. The possibility of extracting parameters of the black hole system from the model is presented and the possibility of including modelling of different disk geometries into the here developed approach is briefly sketched.
In summary, the method developed within the frame of this thesis allows for modelling of the illumination of the accretion disk by a general photon source in Kerr-spacetime and can be used to physically model the source geometry by comparison with observations.

# Contents

# 1. Introduction

Ever since they were first suggested by the Schwarzschild solution to Einsteins Field equations (Schwarzschild 1916), black holes puzzled the scientific community. As per their defining properties, they constitute a region in spacetime that by no means can be tested directly. Only their effects on the surrounding environment can be tested and conclusions on the inner workings must be derived from this data indirectly.

Being the cause of many paradoxes (such as the still unresolved information loss paradox and the firewall paradox), the existence of black holes was rejected by the scientific community at first. The first hard evidence for their existence however was found by Murdin & Webster (1971) and Webster & Murdin (1972) by investigating Cygnus X-1. Nowadays, the number of black holes inside the milky way galaxy alone is estimated to be above ten million (Nagaraja 2019). On April 10th 2019, the Event Horizon Telescope (EHT) obtained the first ever direct visual evidence for a supermassive black hole (Messier 87). A supermassive black hole (SMBH) is a type of black hole, that is typically found at the center of galaxies with typical masses between $10^6$ and $10^9$ $M_\odot$. The other type of black holes is the so called Galactic Black Holes (GBHs), whose typical mass ranges only up to a few tens of solar masses. They are created by supernovae of massive stars. Despite their immense difference in mass, the physical processes associated with SMBHs and GBHs are the same for both types. The main difference of the processes is the scale of their gravitational effects.
In the face of the astounding amount of indications and evidence, the existence of black holes is generally accepted by the scientific community. All the more pressing becomes the question of the nature and mechanisms inherent to such an object.

## 1.1. Black Holes and Accretion

Most of the observable black holes are typically surrounded by a so-called accretion disk, which consists of in-falling matter from the vicinity. There are several descriptions/models for such accretion disks, however Shakura & Sunyaev (1973) presented a widely accepted model based on hydrodynamics without magnetic fields (see also Novikov & Thorne, 1973). This model is also called the Shakura-Sunyaev-Disk (SSD) or Standard Disk. In the SSD model, the in-falling matter is spiraling around the central black hole in a geometrically thin, but optically thick disk. The qualitative flow of the matter can be explained as follows: A particle within the flow may have a certain angular momentum and the according angular velocity around the accreting object. As the matter in the accretion disk flows turbulently, rubs and bounces may reduce the particles angular momentum, thereby reducing its angular velocity. Magneto-hydrodynamic considerations show that the turbulence in the disk and shear forces due to small magnetic fields can create an effective viscosity of the disk material which can be used to transport the deprived angular momentum outwards (see also Krolik 1999; Krishan & Mahajan 2008, Balbus & Hawley 1991) The lower angular momentum then forces the particle to move

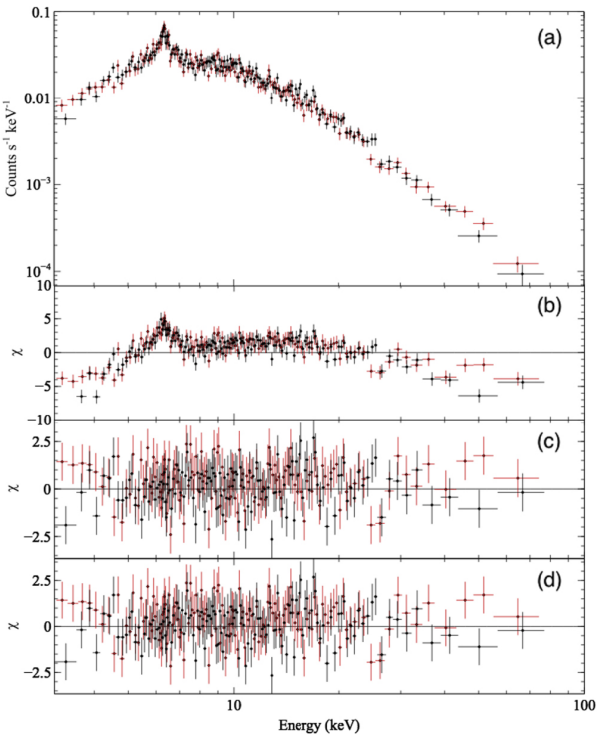


**Figure 1.1:** Folded *NuSTAR* energy spectrum of NGC 4388 (a) alongside fit residuals for (b) a simple power-law model, (c) an absorbed power law with an Fe K$\alpha$ line, (d) an absorbed power law with Fe K$\alpha$ line and a reflection component incorporated using the pexrav model. Black points correspond to FPMA data while points in red correspond to FPMB. Figure taken from Kamraj et al. (2017)

into an orbit closer to the central object, acquiring kinetic energy from falling into the gravitational potential in the process. In total, the particle has thus lost energy and angular momentum, travels on an orbit closer to the black hole and has gained speed. Through this higher speed, frictional heating is increased. Hence, the disk has its highest temperatures at its innermost region. The maximal temperature can be up to a few $10^8$ K (Shakura & Sunyaev 1973). Hence the matter flow is believed to consist mainly of ionized material, or plasma, which explains the above mentioned property of the disk to be optically thick/opaque.

Due to the high temperature and high optical depth, the accretion disk is expected to emit black body radiation. As the temperature for an optically thick disk decreases with the distance from the black hole as $r^{-3/4}$ (Shakura & Sunyaev 1973) the spectrum resembles a stretched black body spectrum. The observed spectrum shows a strong component in high X-ray energies additionally to the thermal contribution. The shape of this additional component can be approximated by a power law $E^{-\Gamma}$ with the so called 'photon index' $\Gamma$. The energy spectrum of the Seyfert-2 galaxy NGC 4388 taken by *NuSTAR* on Dec. 27 2013 is depicted in Fig. 1.1. Though the origin of this power law contribution is not yet determined, the prevailing theory assumes that thermal photons

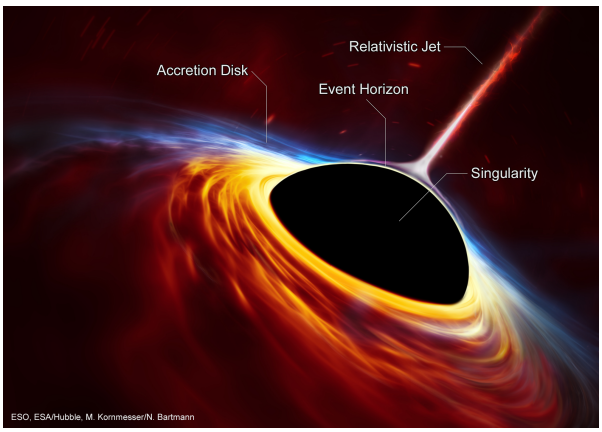


**Figure 1.2:** Artists rendition of a black hole and the surrounding accretion disk, emitting a relativistic jet. Credit: Illustration: ESO, ESA/Hubble, M.Kornmesser/N.Bartmann; Labels: NASA/CXC

emitted from the disk are inverse-Compton up-scattered in a corona of hot electrons (Sunyaev & Truemper, 1979) and reilluminate the accretion disk, leading to multiple absorption and emission features. This will be touched upon further in Sec. 1.3.

As observed with many stellar objects, surrounded by an accretion disk, the region around a black hole can emit an astrophysical jet, which is an outflow of ionized matter in the form of an extended beam along the axis of rotation. The nature and formation of such jets is not yet completely understood, however, the formation of a jet is believed to be linked to the spin parameter $a$ of the black hole (Blandford 1999). An artists illustration of a black hole with accretion disk and relativistic jet is depicted in Fig. 1.2.

## 1.2. The Spin of a Black Hole

Although black holes may seem to be highly complex objects, they indeed rank among the simplest objects in physics. A black hole is completely determined by as few as three parameters: Their mass $M$, the spin parameter $a$ and lastly the electric charge $q$. Even more, the electric charge is in most cases negligible (see e.g., Orito & Yoshimura, 1985). A black hole with a significant electric charge would be neutralized again by vacuum polarization (see Reynolds & Nowak, 2003). So in reality the black hole is completely determined by two parameters $M$ and $a$. The mass is responsible for most of the gravitational effects and can mostly be inferred from the motion of nearby objects (e.g. Orosz et al., 2011) or its effect on photons, i.e., gravitational lensing (for a review, see Bartelmann, 2010). As such, determining the mass of a black hole to a reasonable uncertainty is easily possible.

The spin parameter $a = J/M$, with $J$ being the black holes angular momentum and $M$ its mass, can in principal range from $-1$ to 1. Negative spin parameter in this case means, that the accretion disks angular momentum is antiparallel to the black holes angular momentum. Considering the black hole's interaction with thermal photons from

the accretion disk, Thorne (1974) showed, that the maximal value for $a$ is somewhere below 1, namely $a_{\max} = 0.998$. In turn, this means that the maximal negative value $a$ can take is $-a_{\max} = -0.998$. These are also the maximal/minimal values adopted for the sake of this thesis.

The black hole spin only has noticeable effect at the innermost regions. Hence, the methods for determining the black hole mass are not well suited for the determination of its spin parameter. Still, the importance of $a$ becomes clear, when reminded of the discussion in the previous subsection 1.1. The thermal photons are emitted mainly from the inner edges of the disk, meaning that the spin parameter $a$ greatly affects the spectrum received from the inner region around a black hole. In order to understand the additional component at high X-ray energies, understanding and measuring the spin parameter of a black hole is crucial.

The formation of the relativistic jets of black holes may also be linked to the spin parameter. Many models, simulating the formation of such jets (e.g. Blandford & Znajek, 1977), connect the existence and the power of the jet of a black hole to the black hole spin $a$. These considerations lead to the so called 'spin paradigm', which states that (to first order) the value of $a$ determines whether a strong radio jet is produced or not (see Wilson & Colbert, 1995 and Blandford, 1999). On the other hand, Garofalo et al. (2010) argue that the most powerful jets are emitted by black holes with maximal negative spin. A distribution of jet power over black hole spin of several objects might provide further insight and constraints for jet models.

Similarly to the hard X-ray component in the spectrum, the emission lines are greatly influenced by the black hole spin. Since the energy of these lines is well known they are suited to infer the spin parameter from their smearing. As the lines are created in close vicinity to the black hole, relativistic effects that are dependent on $a$ affect the line width, the line position, and the line shape. From this information as well as taking into account the influence of the relativistic effects, the spin parameter can be measured. However, the presumption to do this measurement, namely theoretical knowledge about the formation of the emission line, which includes the disk geometry, the corona geometry and the exact description of the inverse-Compton up-scattering are crucial to draw reliable conclusions from the spectrum. Previous studies have concentrated on a small number of accretion geometries and therefore their uniqueness could degree of conformity could not be tested. Consequently, it is necessary to generalize the existing models.

## 1.3. The Primary Source

As mentioned in the previous section, the spectrum observed from the vicinity of a black hole usually shows significant emission features, which indicates the existence of a hard X-ray source in the proximity of the black hole that illuminates the accretion disk. Initially it was assumed that this source consists of a hot corona around the inner most regions of the accretion disk, leading to inverse-Compton up-scattering of the

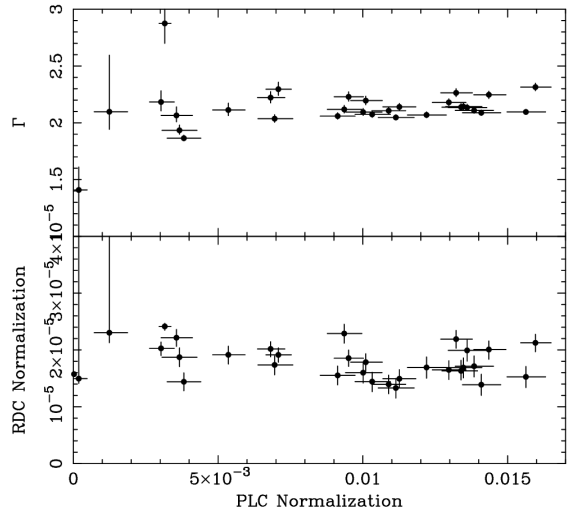


**Figure 1.3:** Photon Index Γ (upper panel) and reflection strength RDC (lower panel) for varying primary flux (PLC) of MCG–6-30-15. Both parameters show little variation, while the continuum flux varies by large amounts. (Figure adapted from Fabian & Vaughan, 2003.

thermal photons which then re-illuminate the disk. Assuming that the intensity of the re-illumination by the corona is proportional to the disk emissivity, the irradiation of the accretion disk would follow a power law of $I(r) \propto r^{-3}$ at the outer parts of the disk and flatten towards the inner regions.

This corona geometry however faces multiple inconsistencies when compared to observational data. In many observations, the data showed disk emissivities that are much steeper at the inner regions of the accretion disk (see Wilms et al., 2001; Fabian et al., 2002; Brenneman et al., 2011; Gallo et al., 2011; Dauser et al., 2012; Risaliti et al., 2013). Further, one would expect a positive correlation between the continuum flux and the reflected flux. A higher continuum flux indicates higher disk emissivity which means that more photons can be reflected at the corona back onto the disk which leads to a higher irradiation intensity on the disk. This means that a higher continuum flux should also come with a higher emission line flux. Observations of MCG–6-30-15 by Fabian & Vaughan (2003) as well as Miniutti et al. (2003), for example, showed large variation in the continuum flux while the reflected flux stayed constant. The data of Fabian & Vaughan (2003) are depicted in Fig. 1.3.

In contrast, a primary source that is located on the rotational axis of the black hole at a height $h$ can explain the observed data very well (see Martocchia et al., 2002; Fabian & Vaughan, 2003; Miniutti et al., 2003, Vaughan & Fabian, 2004). This geometry is also called the lamp post geometry. Unlike the standard disk corona, the primary source is hereby located on the axis of the black hole. Both the lamp post geometry and the standard disk corona geometry are depicted in Fig. 1.4. In the lamp post geometry, the

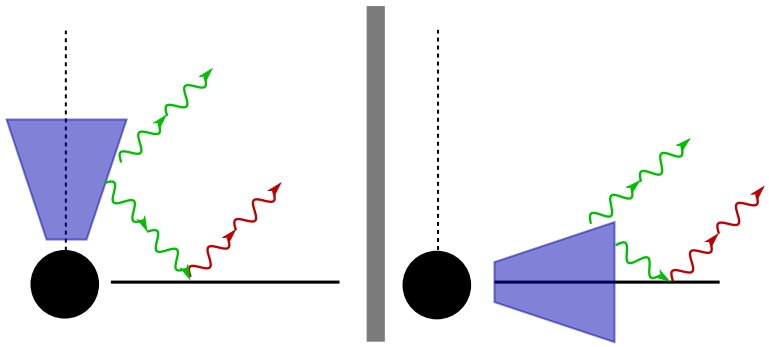

**Figure 1.4:** Sketch of the lamp post geometry (left) and the standard corona geometry (right). The primary source (blue) is located on the rotational axis (left) or encapsulating the accretion disk (right) respectively. A part of the primary photons (green) is emitted towards the observer directly, whereas a part is reflected on the disk and reaches the observer indirectly (red). Image inspired by Dauser (2014)

steepening of the emissivity profile at the inner regions can be explained by the effects of focusing of the radiation onto the inner parts of the accretion disk due to light bending and the effect of energy shift. The observed relation between the continuum flux and the reflected flux is explained by this picture as well; A primary source located close to the black hole (i.e., small $h$), the photons are strongly focused on the inner parts of the accretion disk, creating a strong reflection component and leaving fewer photons for the continuum flux (Miniutti & Fabian, 2004). For increased height $h$ of the X-ray source, the focusing becomes less prevalent, meaning that more photons can escape, thereby enhancing the continuum flux (Miniutti & Fabian, 2004).

## 1.4. Aim of this Thesis

There exist several tools for calculating the spectrum of an irradiated accretion disk from a Jet-Base corona (see Dauser et al., 2013; García et al., 2014; Fukumura et al., 2009), as well as some tools for the simulation of the spectra of extended sources (see e.g. Wilkins & Fabian, 2012). The former lack the ability to investigate corona geometries that are not located on the axis of symmetry, while the latter lack in speed as they commonly use Monte Carlo simulations on graphic cards to compute the spectra. For fitting simulated spectra to observed data, both the computational speed and the possibility to modify the corona geometry is necessary. The model presented in this thesis aims at meeting both of these requirements and ultimately obtain the spectra for various geometries and parameter in a way that is suitable for comparing them to observations.

The remainder of this thesis is structured as follows. In Chapter 2 the derivation of the Kerr-spacetime is briefly outlined. The equations of motion for a massless particle are given in Section 2.3 and the motion of the accretion disk is discussed in Section 2.4. Chapter 3 is divided into two parts; The first part, Section 3.1 summarizes the treatment of the lamp post geometry. The second part, Section 3.2 generalizes the treatment of the

first part to emission from an arbitrary source by following the work of Yang & Wang (2013). In the same way as Chapter 3 is divided into lamp post geometry and general approach. The results are presented and compared in 4 in two Sections; The results for the lamp post geometry are presented in Chapter 4.2, together with the comparison to previous work of Dauser (2014). Section 4.3 then presents the results for some off-axis geometries as examples for which comparative data was partially available. Finally, the conclusion and a further outlook are given in Chapter 5.

# 2. Basic Theory of Black Holes

In 1916, barely over a month after the publication of Einstein's theory of general relativity, famous German physicist Karl Schwarzschild presented a solution to Einsteins Field Equations assuming a spherically symmetric and static vacuum. This solution is best known as the outer Schwarzschild solution or the outer Schwarzschild metric. Remarkably, if the object sourcing the above mentioned gravitational field is compact enough, there exists a region in spacetime from which neither massive nor massless worldlines can escape. This region is called a black hole. Its boundary is called the event horizon of the black hole. The ability to permit black holes is not unique to the Schwarzschild solution but was found even in a family of solutions to the Einstein field equations, namely the Kerr Solution (Kerr, 1963) and the Kerr-Newman solution (Newman et al., 1965). The derivation of the former will be presented in the following. Due to its relevance for the description of most known black holes, it will be at the center of this thesis.

For readers well versed in the formalism of general relativity and black hole physics, some of the following sections may be omitted, as their content is usually covered by any standard textbook on black holes (e.g. Misner et al. 1973; Carter 1968; Kerr 1963). In particular the derivation in the following chapters is based on Chandrasekhar (1983). However, not exclusively but especially for readers not accommodated in the field, it is instructive to read the following chapter to clear up any possible confusion arising by notation or definitions. As such by defining the assumption of stationary spacetime in terms of mathematical expressions avoids the danger of using ones own intuition or possibly textbooks with other definitions of such terms to understand the issue at hand.

## 2.1. Derivation of the Kerr metric

A general and exact solution to the Einstein field equations has not yet been found. However, under certain symmetry assumptions, it is indeed possible to systematically derive exact solutions. For example to obtain the Schwarzschild metric, a static, spherically symmetric vacuum is assumed. In the following, we will loosen the assumption on spherical symmetry and staticity to only axial symmetry and stationarity, which allows for consideration of non-vanishing angular momentum of the central object. This is a very necessary generalization, as during stellar collapse and the formation of black holes, the angular momentum is conserved and transfers onto the resulting black hole. Thus, black holes in reality are expected to have non-vanishing angular momentum.

In the following, the sketched procedure to deriving the Kerr solution is in spirit analogous to a possible derivation of the Schwarzschild solution however the technicalities are more sophisticated. Starting with the sought after metric tensor g in its most general form, the symmetry conditions are applied and g is regarded in a suitable chart. Then the coefficients of the Christoffel Symbols and the Ricci tensor are calculated from this constrained form of the metric tensor and lastly all found expressions inserted into the Einstein field equations. This will provide the final set of conditions on the metric tensor

g to uniquely determine it.

As mentioned above, we may start with a general metric g, which is supposed to be the solution to the Einstein field equations under the aforementioned symmetry conditions of a stationary and axisymmetric spacetime. The requirement of stationarity translates to the existence of a timelike Killing vector $\xi$ , whereas axial symmetry corresponds to the existence of a Killing vector $X$ with spacelike, closed orbits and the requirement of both symmetries simultaneously also enforces the compatibility condition that the Lie-derivative $\mathcal{L}_\xi X = 0$. These chart independent assumptions are equivalent to the requirement that, at least locally, a coordinate system $(t, \phi, x^1, x^2)$ exists in which the components of the metric are independent of $t, \phi$, that is $g_{ab}(r, \phi, x^1, x^2) = g_{ab}(x^1, x^2)$ (see Ludvigsen 1999). In contrast to the assumptions used for deriving the Schwarzschild metric, here the metric tensor is supposed to only be invariant under simultaneous inversion of the $t$ and the $\phi$ coordinate. Explicitly in the aforementioned coordinate system this means that for the coordinate transformation $(t, \phi, x^1, x^2) \to (-t, -\phi, x^1, x^2)$, the metric components are invariant. Since under this transformation it is always true that $g_{02} \to -g_{02}, g_{03} \to -g_{03}$ and $g_{12} \to -g_{12}, g_{13} \to -g_{13}$, we find that these components must vanish (as well as the components with the indices switched, as $g_{ab}$ is symmetric). What remains is the line element

$$\mathrm{d}s^2 = g_{00}\mathrm{d}t^2 + 2g_{01}\mathrm{d}\phi\mathrm{d}t + g_{11}\mathrm{d}\phi^2 + [g_{22}(\mathrm{d}x^2)^2 + 2g_{23}\mathrm{d}x^2\mathrm{d}x^3 + g_{33}(\mathrm{d}x^3)^2]. \tag{2.1}$$

It can be shown that the expression in square brackets can be brought to a 'diagonal' form (see Chandrasekhar 1983, or Appendix A), such that the line element may be written as

$$\mathrm{d}s^2 = -e^{2\nu}(\mathrm{d}t)^2 + e^{2\psi}(\mathrm{d}\phi - \omega\mathrm{d}t)^2 + e^{2\mu_2}(\mathrm{d}\tilde{x}^2)^2 + e^{2\mu_3}(\mathrm{d}\tilde{x}^3)^2, \tag{2.2}$$

where $\nu, \psi, \omega, \mu_2$ and $\mu_3$ are functions of the coordinates $\tilde{x}^2, \tilde{x}^3$ and $\mu_2$ and $\mu_3$ are free to be restrained by a coordinate choice. The line element in equation (2.2) is often referred to as the standard form of the line element of a general axisymmetric and stationary spacetime.

Fundamentally, the only further information required to deriving the specific stationary, axisymmetric, vacuum solution known as the Kerr solution is the use of the vacuum Einstein field equations, that is

$$R_{ab} - \frac{1}{2}g_{ab}R = G_{ab} = 0 \tag{2.3}$$

and a practical choice of coordinate condition on $\mu_2$ and $\mu_3$. As it is not very instructive to work through the multitude of simplifications of equations derived from the vacuum Einstein field equations, it suffices here to regard the choice of coordinate condition forced on $\mu_2$ and $\mu_3$.

The particular choice of gauge presented below in fact implies no loss of generality (see Chandrasekhar 1983), however it is strongly motivated by physical reasoning. Conveniently, the polar angle $\theta$ with respect to the axis of symmetry is chosen as $\tilde{x}^3$ and $\tilde{x}^2$

will from now on be denoted as $r$. The sought after metric is desired to admit an event horizon, that is, a smooth null-surface. This definition is compatible with the one made earlier in this chapter. Considering a general 2-dimensional null-surface, its equation may be given in the form

$$N(x^1, x^2) = 0, \tag{2.4}$$

and the condition that it be null is

$$g^{ab} N_{,a} N_{,b} = 0 \qquad a, b = 1, 2 \tag{2.5}$$

for a smooth function $N$. The null condition in other words means that the surfaces normal vectors at every point are null. The vectors $\eta$ tangent to the null-surface obey the condition $g^{ab}\eta_a N_{,b} = 0$ by definition. Thus, $N_{,a}$ itself is a tangent vector, i.e. $N_{,a} = g_{ab}\frac{\mathrm{d}\gamma^b(t)}{\mathrm{d}t}$ for some curve $\gamma(t)$ that lies inside the null-surface. Thus at every point of the surface, there exists a tangent vector $\xi$ for which $\xi^a\xi_a = 0$. As a geometrical interpretation, along this direction, the null-surface at every point is tangent to the light cone at that point. Consequently, the light cone lies completely on one side of the null-surface and is at that point tangent to it. The smoothness of both, the function $N$ and the metric tensor field $g$ now also show that all the light cones along the null-surface lie on the same side. The future-pointing world line of a massive or massless particle can thus only cross the null-surface in one direction and hence the null-surface forms an event horizon as characterized earlier in this chapter. Note that for the sake of generality, a 2-dimensional null-surface was considered. Commonly, an event horizon in 4-dimensional spacetime refers to a 3-dimensional null-surface, however a 3-dimensional null-surface automatically contains a 2-dimensional hypersurface that is null. As such, considering a 2-dimensional null-surface retained generality in this case and as shown in Chandrasekhar (1983), existence of such a surface indeed does not specialize the case whatsoever.

As our particular spacetime of interest was enforced axisymmetry about the $\phi$-coordinate as well as stationarity, the function describing the surface of the event horizon is solely dependent on the coordinates $r, \theta$, so it has the form

$$N(r, \theta) = 0, \tag{2.6}$$

for some smooth function $N$ and the tangent space of the surface at each point is spanned by the two vectors $\frac{\partial}{\partial t}$ and $\frac{\partial}{\partial \phi}$. Again the condition, that the surface be null is

$$g^{ab} N_{,a} N_{,b} = 0 \qquad a, b = r, \theta, \tag{2.7}$$

and for the standard form of the metric of an axisymmetric, stationary spacetime, this takes the form

$$e^{2(\mu_3 - \mu_2)}(N_{,r})^2 + (N_{,\theta)})^2 = 0. \tag{2.8}$$

Using the special choice of gauge, let

$$e^{2(\mu_3 - \mu_2)} = \Delta(r), \tag{2.9}$$

where $\Delta(r)$ is some function of $r$, for now unspecified. From Eq. (2.8) it then follows that the equation of the null-surface is given by

$$\Delta(r) = 0. \tag{2.10}$$

Employing the second condition, namely that the surface be spanned by $\frac{\partial}{\partial t}$ and $\frac{\partial}{\partial \phi}$ requires that the determinant of the metric of the subspace $(t, \phi)$ vanish on the surface. Thus,

$$e^{2\psi+2\nu} = 0 \qquad \text{on the null-surface} \tag{2.11}$$

Since $\Delta(r)$ was left unspecified, suppose that

$$e^{\psi+\nu} = \Delta^{1/2} f(\theta), \tag{2.12}$$

i.e. that it is separable in the variables $r$ and $\theta$ with some function $f(\theta)$ that is regular on the entire null-surface. Using parts of the vacuum Einstein field equation

$$R_{11} + R_{00} \equiv 0 + 0 = 0, \tag{2.13}$$

together with Eq. (2.9) and (2.12) and the requirements of regularity of $f(\theta)$ and the convexity of the event horizon, it follows

$$\Delta_{,r,r} = 2 \qquad \text{and} \qquad f(\theta) = \sin(\theta). \tag{2.14}$$

Thus $\Delta(r)$ can be written as

$$\Delta(r) = r^2 - 2Mr + a^2, \tag{2.15}$$

where $M$ and $a$ here appear merely as constants of integration, however they acquire a physical meaning of the mass and the angular momentum per unit mass of the black hole, when later the limits of the Kerr solution are investigated. So with this particular choice (again this choice conserves the generality of the situation, see Chandrasekhar 1983) which is consistent with the existence of an event horizon,

$$e^{\mu_3-\mu_2} = \Delta(r)^{1/2} \qquad \text{and} \qquad e^{\psi+\nu} = \Delta(r)^{1/2}\sin(\theta) \tag{2.16}$$

Completing the derivation of the Kerr solution, the end result can be expressed by the line element as

$$\mathrm{d}s^2 = -\Sigma\frac{\Delta}{\rho^2}(\mathrm{d}t)^2 + \frac{\rho^2}{\Sigma}\left(\mathrm{d}\phi - \frac{2aMr}{\rho^2}\mathrm{d}t\right)^2 \sin^2(\theta) + \frac{\Sigma}{\Delta}(\mathrm{d}r)^2 + \Sigma(\mathrm{d}\theta)^2, \tag{2.17}$$

where $\Sigma = r^2 + a^2\cos^2(\theta)$, $\Delta = r^2 - 2Mr + a^2$ and $\rho^2 = (r^2 + a^2)^2 - a^2\Delta\sin^2(\theta)$. The functions $e^{2\nu}, e^{2\psi}, e^{2\mu_2}$ and $e^{2\mu_3}$ for which the standard form of the line element of a

general axisymmetric and stationary spacetime (Eq. (2.2)) turns into the Kerr solution can now be identified by comparing the coefficients of Eq. (2.2) and (2.17). Substituting

$$\begin{aligned} e^{2\nu} &= \frac{\Sigma\Delta}{\rho^2} \\ e^{2\psi} &= \frac{\rho^2 \sin^2(\theta)}{\Sigma} \\ e^{2\mu_2} &= \frac{\Sigma}{\Delta} \\ e^{2\mu_3} &= \Sigma \\ \omega &= \frac{2aMr}{\rho^2} \end{aligned} \tag{2.18}$$

in Eq. (2.2) then yields the Kerr line element.

As announced earlier, investigating the limits of the Kerr solution gives a physical meaning to the constants $a$ and $M$. Letting $r \to \infty$, the Kerr solution element approaches the Schwarzschild solution

$$\mathrm{d}s^2_{\text{Schwarzschild}} = -\left(1 - \frac{2M}{r}\right)\mathrm{d}t^2 + \frac{1}{1-\frac{2M}{r}}\mathrm{d}r^2 + r^2\mathrm{d}\theta^2 + r^2\sin^2(\theta)\mathrm{d}\phi^2, \tag{2.19}$$

meaning that at a point sufficiently far away from the central mass, the Schwarzschild and the Kerr metric are identical. Thus it immediately follows that the Kerr solution is asymptotically flat as well. Further, in this limit, $M$ takes the same role as the mass of the gravitating object appearing in the Schwarzschild solution, so we also identify $M$ in the Kerr solution (2.17) as the gravitating mass of the black hole. The limit $a \to 0$ also yields the Schwarzschild solution, which describes the gravitational field of a non-rotating body. Thus, $a$ is related to the angular momentum of the black hole and a closer investigation of Eq. (2.17) permits the physical interpretation as the angular momentum per unit rest mass of the black hole.

From the explicit form of the Kerr metric in Eq. (2.17), the condition $\Delta(r) = 0$ for the event horizon can be evaluated. As $\Delta = r^2 - 2r + a^2$ is a quadratic polynomial, its roots are

$$r_\pm = 1 \pm \sqrt{1 - a^2}. \tag{2.20}$$

Thus, in general, the Kerr spacetime has two separate event horizons. The outer event horizon $r_+$ is the one that determines the size of the black hole. As such, if the size of the black hole is mentioned in any of the following parts, it refers to the outer event horizon at $r_+ = 1 + \sqrt{1-a^2}$. The inner horizon at $r_- = 1 - \sqrt{1-a^2}$ constitutes a Cauchy horizon. Within the region enclosed by this horizon, closed time-like curves can exist.

Lastly we turn our attention to the fact that the coefficient in front of $\mathrm{d}\phi\mathrm{d}t$ in (2.17) is unequal to zero for non-vanishing angular momentum. This is a key feature of the Kerr solution (or more generally of a general axisymmetric, stationary solution of the Einstein field equations) and leads to interesting effects.

## 2.2. Frame Dragging Effect

The effect of frame dragging due to non-vanishing angular momentum of the black hole will be discussed in terms of the general axisymmetric, stationary solution of the Einstein field equations Eq. (2.2), at the end however, the specialization to the case of the Kerr solution is trivial and will briefly be mentioned as well.

From (2.2) the basis vectors

$$\begin{aligned} e_{(0)i} &= (\ -e^{\nu}\ , 0\ , 0\ , 0\ ) \\ e_{(1)i} &= (-\omega e^{\psi}, e^{\psi}, 0\ , 0\ ) \\ e_{(2)i} &= (\ \ 0\ \ , 0\ , e^{\mu_2}, 0\ ) \\ e_{(3)i} &= (\ \ 0\ \ , 0\ , 0\ , e^{\mu 3}) \end{aligned} \tag{2.21}$$

form a tetrad frame. To distinguish tetrad frame indices from coordinate indices, the tetrad indices are denoted in brackets. The corresponding covariant form then becomes

$$\begin{aligned} e_{(0)}{}^{i} &= (e^{-\nu}, \omega e^{-\nu}, \ 0\ \ , \ 0\ ) \\ e_{(1)}{}^{i} &= (\ 0\ , e^{-\psi}\ , \ 0\ \ , \ 0\ ) \\ e_{(2)}{}^{i} &= (\ 0\ , \ \ 0\ \ , e^{-\mu_2}, \ 0\ ) \\ e_{(3)}{}^{i} &= (\ 0\ , \ \ 0\ \ , \ 0\ \ , e^{-\mu_3}) \end{aligned} \tag{2.22}$$

It is now easy to verify, that

$$e_{(a)}{}^{i} e_{(b)i} = \eta_{(a)(b)} = \begin{pmatrix} -1 & 0 & 0 & 0 \\ 0 & 1 & 0 & 0 \\ 0 & 0 & 1 & 0 \\ 0 & 0 & 0 & 1 \end{pmatrix} \tag{2.23}$$

which means that in the frame chosen as in Eq. (2.21) the Kerr metric Eq. (2.17) is Minkowskian, that is, this choice of frame locally represents an inertial frame. Let a particle in this initial frame have the velocity

$$u^{(a)} = (1, 0, 0, 0)\,, \tag{2.24}$$

i.e., it is stationary with respect to its own frame of reference. In other words, in this frame the particle is at rest. Its velocity as seen by a distant observer however can be calculated as

$$u^{a} = e_{(i)}{}^{a} u^{(i)} = \left(e^{-\nu}, \omega e^{-\nu}, 0, 0\right). \tag{2.25}$$

Remarkably, the velocity component in rotational direction about the axis of symmetry is non-vanishing. So the velocity, the distant observer sees the particle moving with is

$$\dot{\phi} = \frac{\mathrm{d}\phi}{\mathrm{d}t} = \frac{\mathrm{d}\phi}{\mathrm{d}s}\frac{\mathrm{d}s}{\mathrm{d}t} = \frac{u^{\phi}}{u^{t}} = \omega \propto \frac{2aM}{r^3}. \tag{2.26}$$

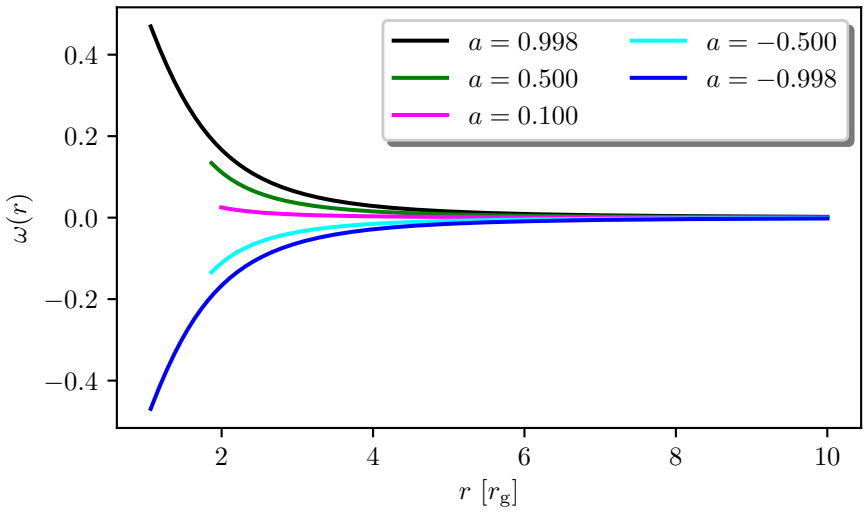


**Figure 2.1:** Velocity $\omega$ due to the effect of Frame Dragging as function of the distance from the black hole for different values of the spin parameter a and in the equatorial plane $\theta = \pi/2$.

This velocity is displayed for different spin parameters in fig. 2.1

A similar, visual display of this effect is the geodesic of a particle with zero angular momentum about the axis of symmetry falling towards the black hole from a far distance. A distant observer will see the particle start to spin about the axis of rotation as it gets closer to the black hole, effectively spiraling towards it instead of falling 'straight' into it. The particle however will feel as if falling straight towards the black hole, the same way a particle would feel falling straight onto earth. An example of this for a photon trajectory starting at $r = 8\ r_g$ with only non-vanishing initial momentum in $r$-direction can be seen in fig. 2.2. The $x$ and $y$ coordinate in this figure are given in terms of gravitational radii, which is given as

$$r_g = \frac{GM}{c^2}, \tag{2.27}$$

where $G \approx 6.67 \cdot 10^{-11} \frac{\mathrm{m}^3}{\mathrm{kg\ s}^2}$ is the gravitational constant, $M$ is the mass of the black hole and $c$ is the speed of light. In the further used natural units, where $G = m = c = 1$, the gravitational radius becomes unity as well.

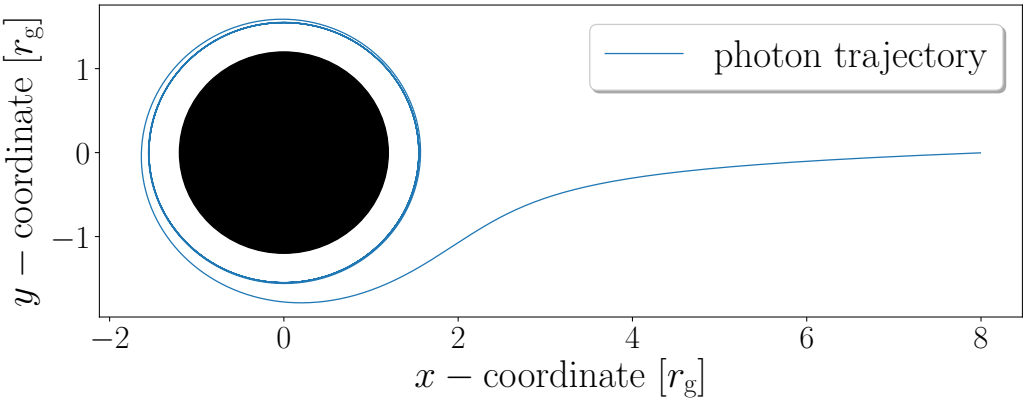


**Figure 2.2:** Frame Dragging effect on a photon trajectory. The plot shows the view of a distant observer on the rotational axis viewing onto the $x$-$y$-plane of the black hole. The photon trajectory starts at $r = 8\ r_g$ with initial momentum solely in $r$-direction. The distant observer however will see the photon start spiraling in $\phi$-direction, due to the effect of frame dragging.

## 2.3. General Equations of Motion

In the theory of general relativity, an uncharged particle, that is a particle free from all external forces, follows a geodesic. Geodesics geometrically generalize the concept of a straight line to curved geometry. The idea that particles follow 'straight' curves is equivalent to the variational principle of Hamiltonian mechanics. A curve $\gamma$ in spacetime is called a geodesic if it satisfies the equation

$$\frac{\mathrm{d}^2 x^a}{\mathrm{d}\lambda} - \Gamma^a{}_{bc} \frac{\mathrm{d}x^b}{\mathrm{d}\lambda} \frac{\mathrm{d}x^c}{\mathrm{d}\lambda} = 0, \tag{2.28}$$

where $x(\lambda)$ is the representation of $\gamma(\lambda)$ in any chart $(U, \mathrm{x})$ and $\Gamma^a{}_{bc}$ are the coefficients of the Christoffel-Symbols, which are the Levi-Civita connection in general relativistic spacetime. The geodesic equation (2.28) is indeed nothing but the Euler-Lagrange equation for the action functional

$$S(g;\gamma] = \frac{1}{2} \int \mathrm{d}\lambda\ g_{\gamma(\lambda)}(\dot{\gamma}(\lambda), \dot{\gamma}(\lambda))\,, \tag{2.29}$$

where the square/round bracket is meant to indicate that the functional $S$ is functionally dependent on the variables appearing after the semicolon and only dependent, but not functionally dependent, on the variables appearing before the semicolon.

Now, as mentioned in section 2.1, the Kerr solution, as any stationary, axisymmetric spacetime, admits two Killing vector fields $\xi$ and $X$. Thus, in local coordinates they fulfill the Killing equation

$$\nabla_{(a} Y_{b)} = 0, \tag{2.30}$$

where $\nabla_a$ is $a$-th component of the covariant derivative and the brackets around the indices indicate symmetrization. It follows that along a geodesic $\gamma = \mathrm{x}^{-1} \circ x$, the quantity

$$Y_a \frac{\mathrm{d}x^a}{\mathrm{d}\lambda} = \text{const.} \qquad \text{where } Y \in \{\xi, X\} \tag{2.31}$$

is conserved. To see this, consider its change along the geodesic

$$\frac{\mathrm{d}}{\mathrm{d}\lambda}\left(Y_a \frac{\mathrm{d}x^a}{\mathrm{d}\lambda}\right) = \frac{\mathrm{d}x^a}{\mathrm{d}\lambda}\nabla_a\left(Y_b \frac{\mathrm{d}x^b}{\mathrm{d}\lambda}\right). \tag{2.32}$$

Due to the product rule for differential operators, the expression on the right side of Eq. (2.32) can be written as

$$\underbrace{\frac{\mathrm{d}x^a}{\mathrm{d}\lambda} Y_b \nabla_a \left(\frac{\mathrm{d}x^b}{\mathrm{d}\lambda}\right)}_{=0 \text{ due to geodesic equation}} + \underbrace{\frac{\mathrm{d}x^a}{\mathrm{d}\lambda}\frac{\mathrm{d}x^b}{\mathrm{d}\lambda}\nabla_a(Y_b)}_{=0 \text{ due to the Killing condition}} = 0. \tag{2.33}$$

So indeed, the claim that for any Killing vector $Y$ satisfying the Killing condition (2.30) the quantity $Y_a \frac{\mathrm{d}x^a}{\mathrm{d}\lambda}$ is conserved along the geodesic $x(\lambda)$. The conserved quantities that arise from the aforementioned $\xi$ and $X$, i.e., from the stationarity and the axisymmetry are the angular momentum $l$ and the energy $E$. From a physical standpoint, the rest mass of a test particle is also expected to be conserved, however this conserved quantity does not follow from a Killing vector, as it is notrelated to a geometrical symmetry.

Mathematically, the conservation of rest mass corresponds to the constancy of the Hamiltonian, which can be derived from Eq. 2.29. The resulting Hamiltonian is

$$H = \frac{1}{2\Sigma}\left(\Delta {p_r}^2 + {p_\theta}^2 - \frac{\rho^2}{\Delta}{p_t}^2 + \left(\frac{1}{\sin^2(\theta)} - \frac{a^2}{\Delta}\right){p_\phi}^2 - \frac{4aMr}{\Delta}p_t p_\phi\right), \tag{2.34}$$

where

$$\begin{aligned}
p_t &= -\left(1 - \frac{2Mr}{\Sigma}\right)\dot{t} - 2Mar\frac{\sin^2(\theta)}{\Sigma}\dot{\phi} \\
p_r &= \frac{\Sigma}{\Delta}\dot{r} \\
p_\theta &= \Sigma\dot{\theta} \\
p_\phi &= \left(r^2 + a^2 + a\frac{\rho^2}{\Sigma}\omega\sin^2(\theta)\right)\sin^2(\theta)\dot{\phi} - \frac{\rho^2}{\Sigma}\omega\sin^2(\theta)\dot{t}.
\end{aligned} \tag{2.35}$$

Since the Hamiltonian is not explicitly dependent on the coordinates $\phi$ and $t$, they are cyclic variables, in agreement with the discussion above about the conserved quantities corresponding to the Killing vector $\xi$ and $X$. Thus, the angular momentum $l$ can be identified as $p_\phi = l$ and the energy can be identified as $-p_t = E$. However, it can also clearly be seen that the Hamiltonian induces the conservation of a test particle's rest

mass. Finally, from this Hamiltonian it is possible to use the Hamilton-Jacobi formalism to extract a further conserved quantity, which was demonstrated by Carter (1968). The conserved quantity

$$\mathcal{Q} = {p_\theta}^2 + \cos^2(\theta)\left[a^2\left(\mu^2 - {p_t}^2\right) + \frac{{p_\phi}^2}{\sin^2(\theta)}\right] \quad \text{where } \mu = \begin{cases} 1 \text{ for massive particles} \\ 0 \text{ for massless particles} \end{cases}, \tag{2.36}$$

is therefore called the Carter constant. It does not arise from a symmetry in the standard sense, but from a separation ansatz in the Hamilton-Jacobi formalism in the coordinates $\theta$ and $r$. Finding a geodesic of a particle in the 4-dimensional spacetime is generically a '*4-dimensional problem*', however due to the four conserved quantities presented above, the geodesic is indeed uniquely determined. Thus, from a theoretical standpoint, the framework is set and the remaining problem is to solve for the respective geodesic.

Following Bardeen et al. (1972) the general equations of motion for a massless particle (i.e. $\mu = 0$ and in natural units G=$M$=c=1) derived from the above are

$$\begin{aligned}
\Sigma\frac{\mathrm{d}t}{\mathrm{d}\sigma} &= -a(aE\sin^2(\theta) - \lambda) + (r^2 + a^2)\frac{T}{\Delta} \\
\Sigma\frac{\mathrm{d}r}{\mathrm{d}\sigma} &= \pm\sqrt{V_r} \\
\Sigma\frac{\mathrm{d}\theta}{\mathrm{d}\sigma} &= \pm\sqrt{V_\theta} \\
\Sigma\frac{\mathrm{d}\phi}{\mathrm{d}\sigma} &= -a\left(a - \frac{\lambda}{\sin^2(\theta)}\right) + a\frac{T}{\Delta},
\end{aligned} \tag{2.37}$$

where $\sigma$ is an affine parameter for massless particles or the proper time for a massive particle and where

$$V_r = r^4 - (q + \lambda^2 - a^2)r^2 + 2\left[q + (\lambda - a)^2\right]r - a^2 q \tag{2.38}$$

$$V_\theta = q^2 + a^2\cos^2(\theta) - \lambda^2\cot^2\theta \tag{2.39}$$

$$T = r^2 + a^2 - \lambda a \tag{2.40}$$

$$\lambda = \frac{l}{E} \qquad q^2 = \frac{\mathcal{Q}}{E^2}. \tag{2.41}$$

The signs in Eq. (2.37) can be chosen independently and represent the direction of the particle's movement. Carter (1968) found these equations of motion to be integrable and

gave the integral form of the equations of motion for a massless particle as

$$\pm \int^{r} \frac{\mathrm{d}r'}{\sqrt{V_r(r')}} = \pm \int^{\theta} \frac{\mathrm{d}\theta'}{\sqrt{V_\theta(\theta')}} \tag{2.42}$$

$$\sigma = \int^{r} \frac{r'^2}{\sqrt{V_r(r')}}\,\mathrm{d}r' + a^2 \int^{\theta} \frac{\cos^2(\theta')}{\sqrt{V_\theta(\theta')}}\,\mathrm{d}\theta' \tag{2.43}$$

$$t = \sigma + 2\int^{r} \frac{r'T}{\Delta\sqrt{V_r(r')}}\,\mathrm{d}r' \tag{2.44}$$

$$\phi = a\int^{r} \frac{T}{\Delta\sqrt{V_r(r')}}\,\mathrm{d}r' + \int^{\theta} \frac{\lambda - a^2\sin^2(\theta')}{\sin^2(\theta')\sqrt{V_\theta(\theta')}}\,\mathrm{d}\theta' \tag{2.45}$$

Solving these equations for the special lamp post Geometry following the work of Dauser (2010) will be the topic of chapter 3.1. Solving these equations for a general photon source will be the topic of 3.2. In both of these cases, the accretion disk of the black hole will be modeled as a standard '*razor thin*' accretion disk. This model and its dynamics will be described in the following section 2.4

## 2.4. Accretion Disk Model

The accretion disk model used in the following chapters assumes a thin disk on a stable orbit in the equatorial plane. This condition immediately implies

$$\dot{\theta} = 0 \qquad \text{and} \qquad \theta = \frac{\pi}{2}. \tag{2.46}$$

From Eq. (2.36) and (2.35) then follows $\mathcal{Q} = q = 0$. Indeed, $q$=0 is both a necessary and a sufficient condition for motion, that initially started in the equatorial plane to remain in it. Further, the disk is most easily modeled by a continuum of particles on circular orbits with different radii. For each of these orbits it must then hold that

$$\ddot{r} = 0, \qquad \dot{r} = 0 \qquad \text{and} \qquad r = \text{const}, \tag{2.47}$$

from which Eq. (2.37) it follows

$$\frac{\mathrm{d}V_r}{\mathrm{d}r} = 0 \qquad \text{and} \qquad V_r = 0. \tag{2.48}$$

These equations can be solved simultaneously for E and $l$, which results in (see Bardeen et al. 1972)

$$\frac{E}{\mu} = \frac{r^{3/2} - 2Mr^{1/2} + aM^{1/2}}{r^{3/4}\left(r^{3/2} - 3Mr^{1/2} + 2aM^{1/2}\right)} \tag{2.49}$$

$$\frac{l}{\mu} = \frac{M^{1/2}\left(r^2 - 2aM^{1/2}r^{1/2} + a^2\right)}{r^{3/4}\left(r^{3/2} - 3Mr^{1/2} + 2aM^{1/2}\right)}. \tag{2.50}$$

This results in an angular velocity of the particles of

$$\Omega = \frac{\mathrm{d}\phi}{\mathrm{d}t} = \frac{\sqrt{M}}{r\sqrt{r} + a\sqrt{M}}, \tag{2.51}$$

which holds for both a '*co-rotating*' as well as a '*counter-rotating*' disk, as for the counter-rotating case, $a$ simply becomes negative. Thus, the four-velocity of the accretion disk becomes

$$u_{\mathrm{disk}} = {u_{\mathrm{disk}}}^{t} \left(\partial_t + \Omega \partial_\phi\right), \tag{2.52}$$

with

$${u_{\mathrm{disk}}}^{t} = \frac{r\sqrt{r} + a\sqrt{M}}{\sqrt{r}\sqrt{r^2 - 3Mr + 2a\sqrt{M}\sqrt{r}}}. \tag{2.53}$$

Following Bardeen et al. (1972), the condition for the particles constituting the disk to be on stable orbits additionally gives the restriction $\frac{\mathrm{d}^2 V_r}{\mathrm{d}r} \leq 0$. This yields the condition

$$r \geq r_{\mathrm{ms}}, \tag{2.54}$$

with

$$\begin{aligned} r_{\mathrm{ms}} &= M\left(3 + Z_2 - \mathrm{sign}(a)\sqrt{(3 - Z_1)(3 + Z_1 + 2Z_2)}\right) \\ Z_1 &= 1 + (1 - a^2)^{\frac{1}{3}}\left[(1 + a)^{\frac{1}{3}} + (1 - a)^{\frac{1}{3}}\right] \\ Z_2 &= \sqrt{3a^2 + {Z_1}^2}. \end{aligned} \tag{2.55}$$

For a maximally rotating, non-rotating and maximally counter-rotating disk this means that the disks cannot approach the black hole closer than

$$r_{\mathrm{ms}} = \begin{cases} 1.24\ r_{\mathrm{g}} & \text{for } a = 0.998 \\ 6\ r_{\mathrm{g}} & \text{for } a = 0 \\ 8.994\ r_{\mathrm{g}} & \text{for } a = -0.998 \end{cases}. \tag{2.56}$$

The radii of the outer and inner event horizon as well as the radius of marginal stability are depicted together in Fig. 2.3.

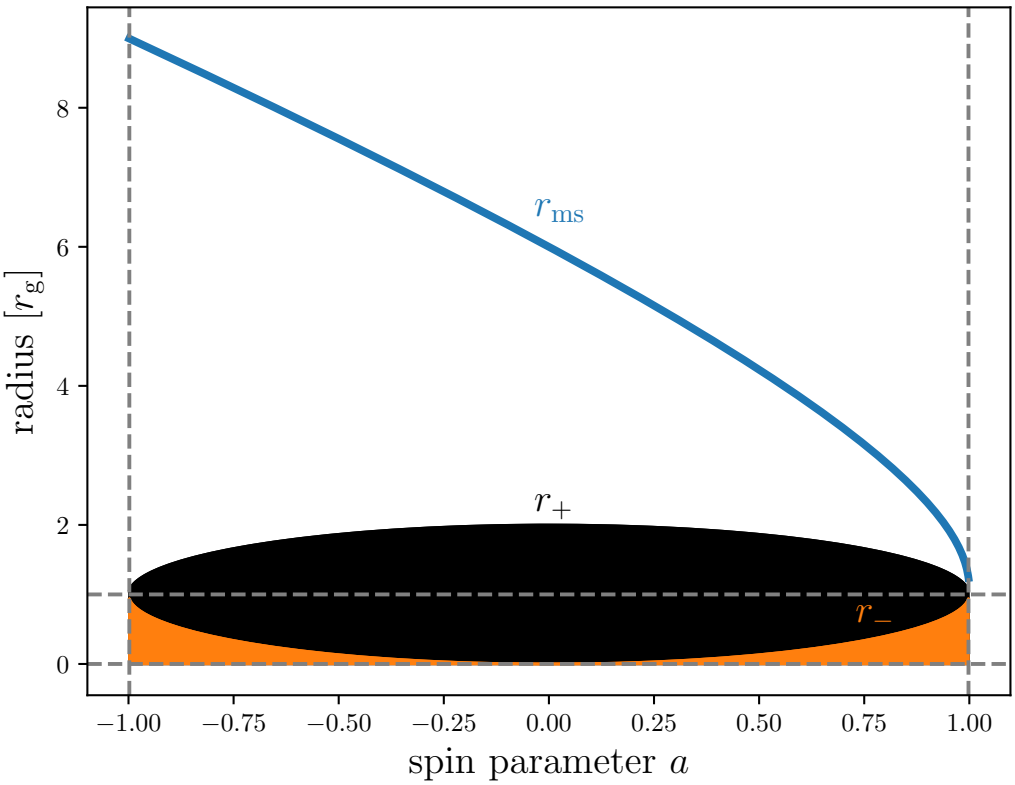


**Figure 2.3:** Outer event Horizon $r_+$, inner event horizon $r_-$ and radius of marginal stability $r_{ms}$ depicted for different spin parameter $a$ from $a = -0.998$ to $a = 0.998$.

# 3. Raytracing

Now that the spacetime of interest has been described, the irradiation of the accretion disk from a photon source can be investigated. The interesting quantity is the incident energy flux on the disk, that is the intensity profile that the photon source causes on the accretion disk. In the first part of this Chapter, the jet-base/lamp post geometry is investigated as an instructive example that simultaneously provides comparative data for the generalized case. The second part will then outline the theory for the calculation of the intensity profile caused by a point source at an arbitrary location in the vicinity of the black hole. The approach to both cases may roughly be outlined as follows: First the equations of motion are reduced and simplified as much as possible such that their integration can be done as quickly as possible. Then the constants of motion are calculated in dependence of the initial data so that the geodesics are completely determined. Lastly the contribution of relativistic effects, such as length contraction and the energy shift along the geodesic is taken into account. Finally, the resulting intensity profile is expressed as a function of the incident photon flux on the disk –

which is calculated from the equations of motion – and the relativistic corrections in the subsequent Chapter 4. The results will hence also be displayed in Chapter 4 for means of comparison and discussion.

## 3.1. Lamp Post Model

Before tackling the calculation of the intensity profile caused by a source located anywhere in the vicinity of the black hole, it is instructive to first consider a simplified case. Equatorial circular motion has already been touched on in Sec. 2.4, when discussing the motion of the accretion disk. The simplification there is that the problem is basically reduced to the $\phi$-direction only, as equatorial motion constrains $\theta$ to be $\pi/2$ and circular motion constrains the $r$-coordinate of the geodesic to be constant as well. As this was already touched on, we may look for another special situation that is easier to calculate than the general case, but still might teach techniques and concepts that are applicable more generally.

A well-developed model for a source of photons in Kerr spacetime is the so called lamp post model. The model assumes an isotropically emitting point source located on the rotational axis of the black hole ($\theta = 0$). The model proves to be a good explanation for the observed focusing on the inner region of the accretion disk as discussed in Sec. 1.3. Further, it has a physical foundation in the base of the jet, emitted by a black hole. The lamp post model is hence worth investigating due to its efficiency in the description of the observed spectra in its own right. Furthermore, it also constitutes a simplification of a general point source in Kerr spacetime, as its location on the axis of symmetry also constitutes a symmetry in the possible trajectories (details on that in Sec. 3.1.1). A heuristic explanation of this simplification can be given by a geometrical consideration. The directions on a sphere may be completely parametrized by the $\theta$- and the $\phi$- direction, or in other terms, the East-West and the North-South direction. For a person standing on the north pole (or on the south pole for that matter), the notion of $\phi$-, or East-West direction no longer makes sense. Each direction the person is looking at is always in $\theta$, or North-South direction. This means that initially, the person on the north pole can not move in the $\phi$-direction, which in turn will lead to them having no angular momentum. Thus, one of the four constants of motion are already determined from the location of the source alone. A more rigorous description, however, will follow in Subsec. 3.1.1.

As the consideration of the lamp post model only serves as an instructive example and provides results for comparisons later on, the treatment will not be as detailed as in papers with their focus on this model. Hence, the interested reader may be referred to the work of Dauser (2010, 2014), Dauser et al. (2013), Fukumura et al. (2009) and García et al. (2014). The following sections on the lamp post geometry are based mainly on Dauser (2010, 2014).

### 3.1.1. Reduced Equations of Motion

The equations of motion for a photon in Kerr spacetime were derived in Subsec. 2.3 and given in Eq. (2.37) and Eq. (2.35) or Eq. (2.42) - (2.45) respectively. If we now consider the case of a source on the rotational axis, the initial condition $\theta = 0$ can be applied. This simplifies the calculation of the initial momenta tremendously, as any term containing only a $\theta$ dependency can immediately be evaluated. However, from the form of the potential $V_\theta$ in Eq. (2.39), it is apparent that we run into difficulties actually applying $\theta = 0$, as the $\cot(0)$ is not defined. Even worse, looking at the $\theta$ equation of Eq. (2.37), for $\lambda \neq 0$ and $\theta \to 0$, the coordinate velocity in $\theta$ direction for any photon emitted in the vicinity of $\theta = 0$ would either be complex or infinite, depending on the sign of $\lambda$. So even the limit of $\theta \to 0$ is unphysical. But it does not seem physically reasonable that photon trajectories can not start from the rotational axis. To avoid divergence of the $\lambda \cot(\theta)$ term, it is necessary that

$$\begin{aligned} &\lim_{\theta\to 0}\left|\frac{\lambda^2}{\sin^2(\theta)}\right| < \infty, \quad \text{and therefore} \\ &\lim_{\theta\to 0} \quad \lambda \quad = 0. \end{aligned} \tag{3.1}$$

The notation ($\lim_{\theta\to 0} x < \infty$) was here used to denote that the term $x$ is not definitely divergent. A direct consequence of this is that any photon emitted by a source on the axis of symmetry must have vanishing angular momentum. This consideration yields a substantial simplification of the equations of motion, as it already determines one of the two important constants of motion to be vanishing. As it is therefore established, that photons originating from the axis of symmetry have vanishing angular momentum $\lambda$ we may for any value of $\theta$ consider only those geodesics with vanishing $\lambda$. The considerations above ensure that no photon geodesic starting at the axis of symmetry is dismissed by restricting concern to this subset of trajectories. Doing so, the potential $V_\theta$ for this subset takes the simpler form of

$$V_\theta(\theta) = q^2 + a^2\cos^2(\theta). \tag{3.2}$$

For this expression the transition to $\theta = 0$ is well-defined and the resulting potential can be expressed as

$$V_\theta(0) = q^2 + a^2, \tag{3.3}$$

for which the root is well defined. We have thus found the description of geodesics with zero angular momentum starting from the rotational axis. As per the previous argument, that for $\lambda \neq 0$ already the limit $\theta \to 0$ leads to unphysical results, the zero angular momentum geodesics are in fact the only geodesics permitted to start from the rotational axis meaning that the vanishing angular momentum requirement meant no restriction for this special case.

As an aside; The problem arises in an analogous fashion to the problem of defining the East-West-direction for a person standing on the north pole, as mentioned earlier. For a photon starting on the rotational axis, the $\phi$-direction simply is not defined and as such, the photon can not move in this (undefined) direction. Further, both of these

problems arise only due to the special choice of coordinates and do not represent any physical limitation on the movement of an object on the rotational axis. As a further remark; Since for each geodesic a point along the geodesic can be regarded as a new starting point for the remainder of the trajectory, it is already conceivable that each photon geodesic running through the rotational axis must be one with vanishing angular momentum. This is true no matter the source geometry.

The above considerations imply that the initial direction of the photon trajectories starting on the axis of symmetry are determined by a single angle $\delta$. From this geometric consideration, the relation between the constant of motion $q$ and the emission angle $\delta$ becomes (Dauser 2010)

$$\sin(\delta) = \frac{(p_h)_a (n_h^{(\theta)})^a}{(p_h)_b (u_h)^b} = \frac{\sqrt{\frac{V_\theta}{\Sigma}}\Big|_{\theta=0}}{-{u_h}^t} = \frac{\sqrt{h^2-2h+a^2}}{h^2+a^2}\sqrt{q^2+a^2}, \tag{3.4}$$

where $n_h^{(\theta)}$ is the normal vector in $\theta$-direction. The non-vanishing component $u_h^t$ of the four velocity can be calculated from the condition

$$1 \stackrel{!}{=} u_a u^a = ({u_h}^t)^2 g_{tt}(h) = -({u_h}^t)^2 \frac{\Delta(h)}{h^2+a^2}. \tag{3.5}$$

Solving Eq. (3.4) for $q$ yields

$$q = \sqrt{\frac{\sin^2(\delta)\,(h^2-2h+a^2)}{h^2+a^2}}. \tag{3.6}$$

Since the angular momentum of the geodesics in the lamp post geometry must be vanishing, the trajectory is completely determined by the constant $q$ and, by means of Eq. (3.6), it is determined by the initial height $h$ above the black hole and the emission angle $\delta$.

With the constants of motion $\lambda$ and $q$ determined from the initial data, the momentum of a photon

$$p_a = E\left(-1, \pm\frac{\sqrt{V_r}}{\Delta}, \pm\sqrt{V_\theta}, \lambda\right) \tag{3.7}$$

is determined and the solution of the equations of motion Eq. (2.42)–(2.45) becomes a problem of numerical integration. This has been done in Dauser (2010), based on the code presented by Speith et al. (1995) for the calculation of Cunningham's transfer function (see also Cunningham, 1975). To calculate the position at which the photon hits the accretion disk, Eq. (2.42) is numerically integrated. For the $\theta$-integration, the lower and the upper limits are known from the initial and incident angle being $\theta = 0$ and $\theta = \pi/2$ respectively. For the $r$-integration, only the lower limit, that is the emission height, is known, whereas the incident radius is sought after. So the value of the upper limit of the $r$-coordinate is gradually increased, until the $r$- and the $\theta$- integrals match (up to a certain precision). The corresponding upper limit $r_{\text{incident}}$ of the $r$-integration is

the radius at which the photon is incident on the disk.

It is hence possible to calculate the radius at which the photon trajectory crosses the accretion disk. Since the situation is symmetric about the rotational axis, the $\phi$-coordinate is of no interest and the $\theta$-coordinate of the incident position is trivially $\pi/2$. By simulating the emission from a source and then numerically solving for the incident radius, a radial distribution of photons incident on the disk can be calculated. Usually, to obtain the intensity distribution, a Monte Carlo simulation of photon trajectories is generated and the amount of photons incident in a within a range of $\Delta r$ are counted. The intensity profile would then arise as the histogram of the amount of photons per radial bin divided by the respective area segment of that bin. However due to relativistic effects, there are multiple corrections that have to be made before creating the histogram. For one, the area corresponding to a radial bin $\Delta r$ is not simply given as $2\pi r\Delta r$ as would be expected from a ring. Instead, following Wilkins & Fabian (2012), the proper area of such a ring at radius $r$ with width $\Delta r$ is given as

$$A(r, \Delta r) = 2\pi \sqrt{\frac{r^4 + a^2 r^2 + 2a^2 r}{r^2 - 2r + a^2}} \Delta r \tag{3.8}$$

in the observer's frame of rest. This effect is displayed in Fig. 3.1.
To calculate the irradiation on the disks surface in the rest frame of the accretion disk, its rotation has to be considered as well. Using the disk velocity given in Eq. (2.51), the corresponding Lorentz factor is given as (Wilkins & Fabian 2012; Bardeen et al. 1972)

$$\gamma^{(\phi)} = \frac{\sqrt{r^2 - 2r + a^2}(r^{3/2} + a)}{r^{1/4}\sqrt{r\sqrt{r} + 2a - 3\sqrt{r}}\sqrt{r^3 + a^2 r + 2a^2}}. \tag{3.9}$$

The effect of the Lorentz contraction due to the rotation of the disk is displayed in Fig. 3.2

With these two corrections, the photon flux on the disk from a monoenergetic source can be calculated from the initial data on the emitting source. The physically interesting quantity however would be the energy flux incident on the disk. Assuming a truly isotropic point source, the energy is evenly distributed into every direction, and as such, each emitted photon starts with the same energy. However, due to relative motion of the emitter as well as general relativistic effects (such as gravitational redshift), the energy of the incident photons may vary. The formula to calculating the resulting energy shift is given in the following section 3.1.2. From there it will be possible to calculate the complete intensity profile on the accretion disk.

### 3.1.2. Energy Shift in the Lamp Post Case

As motivated in the previous section, the energy shift of a photon along its geodesic is necessary to calculate the intensity spectrum on the disk. Fortunately the formulas simplify for the case of the lamp post model. The formula for the general case will be

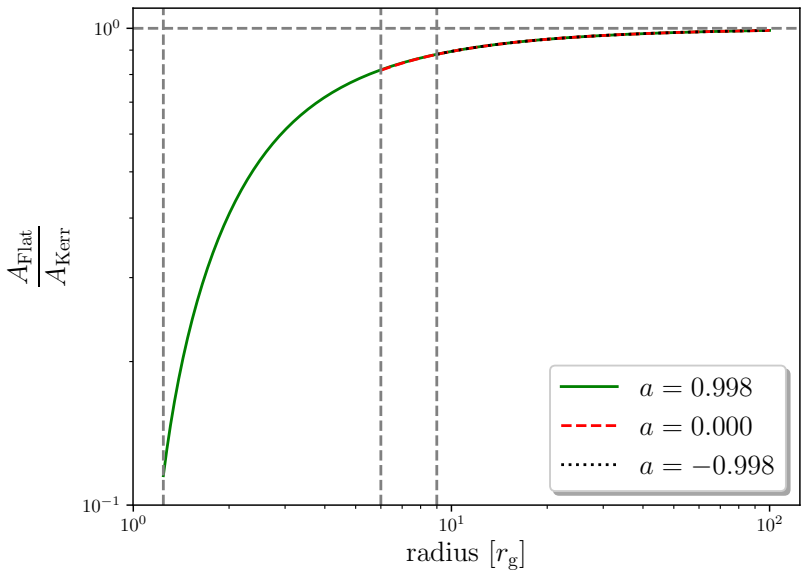


**Figure 3.1:** Correction factor to the area of an annulus of the accretion disk in flat spacetime as a function of the radius for different spin parameters $a$. The correction arises by comparing the area in flat spacetime to the area detected by a distant observer as noted in Eq. 3.8. As expected, the correction has noticeable effect only at the innermost regions of the accretion disk.

derived in Sec. 3.2.5. The initial four-momentum at the primary source is given as

$$u_h{}^a = (u_h{}^t, 0, 0, 0), \tag{3.10}$$

with $u_h^t$ as defined in Eq. (3.5). The corresponding four-momentum on the accretion disk is

$$u_{\text{d}}{}^a = u_{\text{d}}{}^t(1, 0, 0, \Omega), \tag{3.11}$$

as in Eq. (2.51)- (2.53). In combination with Eq. (3.7), the energy shift can be calculated as

$$g = \frac{E_{\text{i}}}{E_{\text{e}}} = \frac{p_a u_{\text{d}}{}^a}{p_b u_h{}^b} = \frac{(r_i\sqrt{r_i} + a)\sqrt{h^2 - 2h + a^2}}{\sqrt{r_i}\sqrt{r_i{}^2 - 3r_i + 2a\sqrt{r_i}\sqrt{h^2 + a^2}}} \tag{3.12}$$

The flux emitted by a physical source is expected to show some kind of energy dependence, more precisely, the X-ray spectra detected from the vicinity of black holes can be described by a power-law of the form $\mathcal{N}(a) = E^{-\Gamma}$, where $\mathcal{N}$ is the photon number density and $\Gamma$ is called the photon index. This dependency has to be modeled as well an can easily be taken care of with the help of the energy shift, by multiplying the overall profile by $g^\Gamma$ instead of $g^1$. The effect of the energy shift is visualized in Fig. 3.3 for emission at height $h = 8\ r_{\text{g}}$ and a spin parameter of $a = 0.998$ and photon indices $\Gamma = 1, 2, 3$. The energy of a photon is related to its frequency by

$$E_{\text{Phot}} = hf, \tag{3.13}$$

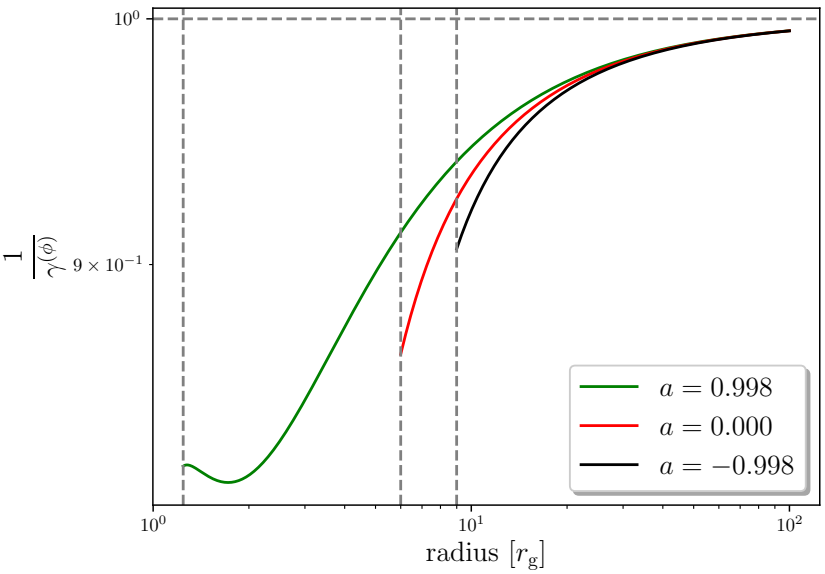


**Figure 3.2:** Correction factor to the area of an annulus of the accretion disk as a function of the radius for different spin parameters $a$. The correction arises due to the rotational velocity of the disk, causing special relativistic Lorentz contraction.

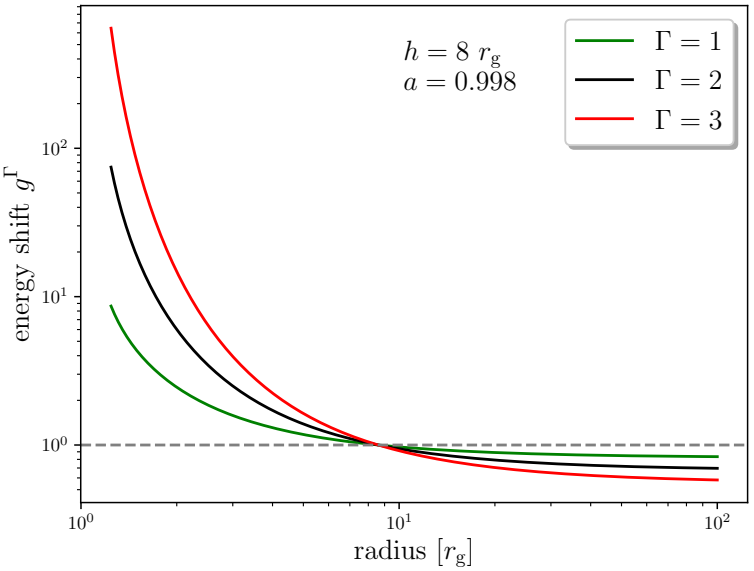


**Figure 3.3:** The energy shift a photon undergoes along its geodesic from its emission point on the rotational axis until it reaches the disk as a function of the incident radius $r$.

where $h$ is the Planck constant and $f$ is the frequency of the photon. Using this relation together with Eq. 3.80 yields

$$f_\mathrm{i} = g f_\mathrm{e}, \tag{3.14}$$

where $f_\mathrm{i}$ is the photon's frequency at impact and $f_\mathrm{e}$ is the photon's frequency at emission. This consideration helps understanding the physical meaning of the energy shift $g$. Photons that reach the disk at the section of the energy shift and the constant 1-line in Fig. 3.3 are neither red- nor blueshifted, i.e., $f_\mathrm{i} = f_\mathrm{e}$. Photons reaching the disk at a radius closer to the black hole – where the energy shift is greater than one – have gained energy along their trajectory and are thus blueshifted, i.e., $f_\mathrm{i} > f_\mathrm{e}$, whereas photons reaching the disk at a farther radius have lost energy along the way and are redshifted, i.e., $f_\mathrm{i} < f_\mathrm{e}$. The section point of the energy shift and the 1-line is approximately at the same radius as the point of emission, which is not surprising. Consider a black hole without angular momentum. The gravitational field generated by such a black hole is spherically symmetric (see Schwarzschild, 1916), as such, the potential energy of a particle at height 8 $r_\mathrm{g}$ and an equal particle on the accretion disk at radius 8 $r_\mathrm{g}$ is the same and thus moving from one place to the other results neither in an energy gain nor loss. So for a black hole with spin parameter $a = 0$, the energy shift becomes unity when the incident radius is equal to the emission radius. Although the angular momentum breaks the spherical symmetry, the effects of the non-vanishing spin parameter are only noticeable at the innermost radii. As such, for emission heights far from the black hole, spacetime can be approximated as spherically symmetric again and the deviations are expected to be negligible. This explains why also in the case for $a = 0.998$ depicted in Fig. 3.3, the energy shift becomes unity at about the same radius as the height of emission.

## 3.2. Raytracing in a Generalized Set-Up

The treatment of the special lamp post geometry in the previous part of this chapter serves multiple purposes in the further development. For one, it is an instructive example how to calculate the intensity profile, in terms of the numerical and analytic methods used. Probably even more important, however, is its purpose as a testing tool for any further machinery developed in this thesis, as the results from any algorithm for the calculation of the intensity profile from a general source geometry must coincide with – or at least resemble – the results obtained from the previous chapter in the case of the lamp post geometry. As such, even though the explicit simplifications and theory developed in chapter 3.1 may not be employable to the general formalism, the detailed analysis will prove to be of much use.

In the following, the theory behind the public *YNOGK*-code provided by Yang & Wang (2013) will be presented following closely their detailed description. This chapter is therefore to be taken as a summary with a few explanatory comments of their work. It is worth mentioning the code of Dexter & Agol (2009), as large parts of the *YNOGK*-code is based on this earlier work. The main difference is the longer runtime of the older code and that information about the turning points has to be provided beforehand in the code of Dexter & Agol.

The approach to solving the equations of motion can be summarized as follows: The coordinates $(t, \phi, r, \theta)$ are expressed by an affine parameter $p$, defined in Eq. (3.15). Thus

the equations of motion themselves are expressed as equations of the constants of motion as well as the affine parameter $p$ only. Subsequently, these emerging 'new' equations of motion are brought to a standard form which can be evaluated using Carlson's method (see Carlson 1989, 1991, 1992). What remains then is the determination of the constants of motion from the initial conditions. This is done by providing an expression of $\lambda$ and $q$ in terms of the affine parameter $p$ as well. The problem of finding the incident radius of a photon on the thin disk from general initial data then becomes a matter of root finding. Finally, the equation for calculating the energy shift a photon undergoes along its way onto the disk is presented and therefore all of the essential parts for constructing the intensity profile are gathered.

To express the coordinates in terms of the parameter $p$ however, it will prove useful to first consider a general property of the photon geodesics. Their turning points with respect to the $r$ and $\theta$ coordinate.

### 3.2.1. Turning Points

From the equations of motion (2.37) it is apparent that $V_r$ and $V_\theta$ must be non-negative. The points where $V_r(r) = 0$ and $V_\theta(\theta) = 0$ are called turning points and their coordinates are denoted by $r_{\mathrm{tp}}$ for turning points in radial direction and $\theta_{\mathrm{tp}}$ for turning points in $\theta$ direction. Due to $V_r$ being solely dependent on $r$ and $V_\theta$ being solely dependent on $\theta$, for a photon emitted at $r_{\mathrm{initial}}$ and $\theta_{\mathrm{initial}}$, its motion is confined between two turning points $r_{\mathrm{tp1}}$ and $r_{\mathrm{tp2}}$ as well as $\theta_{\mathrm{tp1}}$ and $\theta_{\mathrm{tp2}}$. From these turning points, it can be determined whether a photon propagates along a bound or unbound trajectory, i.e., if it stays within a certain distance of the black hole or eventually travels to '*infinity*' or if a photon actually plunges into the black hole. These three cases correspond to $V_r$ either having two real roots $r_{\mathrm{tp1}}$, $r_{\mathrm{tp2}} > r_{\mathrm{EH}}$, a real root $r_{\mathrm{tp1}} < r_{\mathrm{EH}}$ or having no real roots respectively. However, if all turning points $r_{\mathrm{tp}} < r_{\mathrm{EH}}$ are − for our purposes − identified with $r_{\mathrm{EH}}$ and infinity is also regarded as a special turning point in the sense that a photon may approach both these turning points, but never return from them, then canonically, every photon has exactly two turning points in $r$ direction. Without loss of generality, we may require $r_{\mathrm{tp1}} \leq r_{\mathrm{tp2}}$ and $\theta_{\mathrm{tp1}} \leq \theta_{\mathrm{tp2}}$.

Regarding Eq. (2.35) and Eq. (2.37) it immediately follows that for a photon with initial momentum $p_r = 0$ (or $p_\theta = 0$), the potential $V_r$ (or $V_\theta$) vanishes as well and thus $r_{\mathrm{initial}} = r_{\mathrm{tp}}$ (or $\theta_{\mathrm{initial}} = \theta_{\mathrm{tp}}$), meaning that the initial coordinate already constitutes a turning point. Further, Shakura (1987) showed that $\theta = 0$ and $\theta = \pi$ are not roots of $V_\theta$, and thus can not constitute a turning point in $\theta$ direction.

### 3.2.2. Coordinates as Functions of $p$

As already outlined, the first step is to rewrite the coordinates as a function of a parameter $p$. It turns out that defining $p$ from Eq. (2.42), that is

$$p := \pm \int^{r} \frac{\mathrm{d}r'}{\sqrt{V_r(r')}} = \pm \int^{\theta} \frac{\mathrm{d}\theta'}{\sqrt{V_\theta(\theta')}} \tag{3.15}$$

is convenient for that matter. Since in Eq. (3.15) the sign in front of the integral compensate the sign of the differentials under the integral, $p$ is always positive and further, $p$ is monotonically increasing along the geodesic of a photon. The desired outcome of the following calculations is to express the coordinates $t, \phi, r, \theta$ in terms of $p$ using the Weierstrass' and Jacobi's elliptical integrals.

Substituting the coordinate $\theta$ by $\mu := \cos(\theta)$ alters Eq. (3.15) to

$$p = \pm \int^{r} \frac{\mathrm{d}r'}{\sqrt{V_r(r')}} = \pm \int^{\mu} \frac{\mathrm{d}\mu'}{\sqrt{V_\mu(\mu')}}, \tag{3.16}$$

where

$$V_\mu = q - (q + \lambda^2 - a^2)\mu^2 - a^2\mu^4. \tag{3.17}$$

This substitution is useful as now $V_\mu$ is a polynomial in $\mu$. However, it is still cumbersome that $V_r$ and $V_\mu$ are quartic polynomials in $r$ and $\mu$ respectively, whereas the polynomials appearing in Weierstrass' elliptical integral are only cubic. Indeed, Yang & Wang (2013) show that a variable transformation can reduce the polynomials appearing in the square root of the denominator in Eq. (3.16) to cubic polynomials in the new variable. First, define

$$\begin{aligned} b_0 &:= -4a^2{\mu_{\mathrm{tp1}}}^3 - 2(q + \lambda^2 - a^2)\mu_{\mathrm{tp1}} \\ b_1 &:= -2a^2{\mu_{\mathrm{tp1}}}^2 - \frac{1}{3}(q + \lambda^2 - a^2) \\ b_2 &:= -\frac{4}{3}a^2\mu_{\mathrm{tp1}} \\ b_3 &:= -a^2, \end{aligned} \tag{3.18}$$

where $\mu_{\mathrm{tp1}} := \cos(\theta_{\mathrm{tp1}})$. From this, the new variable $\tau$ can be defined as

$$\tau := \frac{b_0}{4}\frac{1}{(\mu - \mu_{\mathrm{tp1}})} + \frac{b_1}{4}. \tag{3.19}$$

The transformation from $\mu$ to $\tau$ results for $p$ in

$$p = \pm \int^{\tau(\mu)} \frac{\mathrm{d}\tau}{\sqrt{4\tau^3 - g_2\tau - g_3}}, \tag{3.20}$$

with

$$g_2 = \frac{3}{4}({b_1}^2 - b_0 b_2)$$
$$g_3 = \frac{1}{16}(3b_0 b_1 b_2 - 2{b_1}^3 - {b_0}^2 b_3)$$

Using the definition of Weierstrass' elliptical function $\wp(z; g_2, g_3)$ from Abramowitz & Stegun (1965), thus from Eq. (3.20) it follows that $\tau = \wp\left(p \pm \Pi_\mu; g_2, g_3\right)$, with

$$\Pi_\mu = \left|\wp^{-1}(\tau(\mu_{\text{initial}}; g_2, g_3)\right|. \tag{3.21}$$

In addition, solving Eq. (3.19) for $\mu$, one can express $\mu$ as a function of p,

$$\mu(p) = \frac{b_0}{4\wp\left(p \pm \Pi_\mu; g_2, g_3\right)}. \tag{3.22}$$

For the practical application, it will of course be crucial to calculate the Weierstrass' elliptic function numerically. Thus the numerical calculation of $\wp(z; g_2, g_3)$ is a central part of the *YNOGK*-code provided by Yang & Wang (2013). The sign in front of $\Pi_\mu$ in Eq. (3.22) depends on the initial four momentum in $\theta$ direction $p_\theta$ as

$$\begin{cases} p_\theta > 0 & & & + \\ p_\theta = 0 & \begin{cases} \theta_{\text{initial}} = \theta_{\text{tp1}} & \Pi_\mu = n\omega & \pm \\ \theta_{\text{initial}} = \theta_{\text{tp2}} & \Pi_\mu = \left(\frac{1}{2} + n\right)\omega & \pm \end{cases} & , \\ p_\theta < 0 & & & - \end{cases} \tag{3.23}$$

with $\omega$ being the period of $\wp(z; g_2, g_3)$ and $n \in \mathbb{N}$. The sign in front of $\Pi_\mu$ for the case $p_\theta = 0$ does not matter and is taken to be positive.

The reader may have noticed that the variable transformation indeed assumed at least one turning point in *theta* direction (see Eq. 3.18), however from Eq. (3.17) it is clear that at least one real root exists and thus at least one real turning point exists.

The same can not be said about $V_r$. So the approach to express $r$ as a function of $p$ will have to also consider the case that $V_r = 0$ has no real solutions $r_{\text{tp}}$. This will be done by involving the Jacobi's elliptic functions $\text{sn}(z|k^2)$ and $\text{cn}(z|k^2)$.
First, regarding the case that the equation $V_r = 0$ as real roots, then $r_{\text{tp1}}$ exists and the variable transition can be made analogously to the variable transition for the $\theta$ coordinate, that is

$$c_0 := 4{r_{\text{tp1}}}^3 - 2(q + \lambda^2 - a^2)r_{\text{tp1}} + 2\left[q + (\lambda - a)^2\right]$$
$$c_1 := 2{r_{\text{tp1}}}^2 - \frac{1}{3}(q + \lambda^2 - a^2)$$
$$c_2 := \frac{4}{3}r_{\text{tp1}}$$
$$c_3 := 1 \tag{3.24}$$

helps define the new variable

$$\kappa := \frac{c_0}{4}\frac{1}{(r - r_{\mathrm{tp1}})} + \frac{c_1}{4}. \tag{3.25}$$

Now similar to the $\mu$-transformation, the $r$-part of Eq. (3.16) turns into

$$p = \pm \int^{\kappa(r)} \frac{\mathrm{d}\kappa}{\sqrt{4\kappa^3 - h_2\kappa - h_3}}, \tag{3.26}$$

with

$$\begin{aligned} h_2 &= \frac{3}{4}\left({c_1}^2 - c_0 c_2\right) \\ h_3 &= \frac{1}{16}\left(3c_0 c_1 c_2 - 2{c_1}^3 - {c_0}^2 c_3\right). \end{aligned} \tag{3.27}$$

Again, taking the inverse of Eq. (3.26), the new variable is obtain as a function of $p$, that is $\kappa = \wp(p \pm \Pi_r; h_2, h_3)$. And – also analogously to the treatment of the $\mu$ transformation – solving Eq. (3.25) for $r$,

$$r(p) = \frac{c_0}{4\wp(p \pm \Pi_r; h_2, h_3) - c_1} + r_{\mathrm{tp1}}, \tag{3.28}$$

with

$$\Pi_r = \left|\wp^{-1}\left(\kappa(r_{\mathrm{initial}}; h_2, h_3)\right)\right| \tag{3.29}$$

is obtained. The sign in front of $\Pi_r$ is dependent on the initial momentum in $r$ direction in the same way as the sign in front of $\Pi_\mu$ was dependent on the initial momentum in $\theta$-direction. So if $V_r = 0$ has real roots, the treatment of the $r$ coordinate is also finished here. However, as already mentioned, this is not necessarily the case.

Considering the case that $V_r$ has no real roots, the goal is then to express $r$ via Jacobi's – rather than Weierstrass' – elliptic function. From Vieta's rules it is now clear that for the roots $r_1, r_2, r_3, r_4$ of the polynomial $V_r$ satisfy

$$r_1 + r_2 + r_3 + r_4 = -a_3 = 0, \tag{3.30}$$

as the cubic contribution in $V_r$ is vanishing. Using this condition together with the knowledge that complex roots only appear in conjugate pairs, the roots can be rewritten as

$$\begin{aligned} r_1 &= u - iw & r_2 &= u + iw \\ r_3 &= -u - iv & r_4 &= -u + iv. \end{aligned} \tag{3.31}$$

Now, define

$$\lambda_{1/2} = \frac{1}{2w^2}\left[4u^2 + v^2 + w^2 \pm \sqrt{(4u^2 + w^2 + v^2)^2 - 4w^2v^2}\right], \tag{3.32}$$

for which $\lambda_1 > 1 > \lambda_2$ and a new variable

$$\epsilon := \sqrt{\frac{\lambda_1 - 1}{(\lambda_1 - \lambda_2)\left[(r-u)^2 + w^2\right]}} \left( r - u\frac{\lambda_1 + 1}{\lambda_1 - 1} \right). \tag{3.33}$$

Transforming from $r$ to the variable $\epsilon$, the $r$-part of Eq. (3.16) becomes

$$p = \int^{\epsilon} \frac{1}{w\sqrt{\lambda_1}\sqrt{(1-\epsilon^2)\left(1 - \frac{\lambda_1-\lambda_2}{\lambda_1}\epsilon^2\right)}}\, \mathrm{d}\epsilon, \tag{3.34}$$

which is the standard Legendre elliptic function. Using the definition of Jacobi's elliptic function $\mathrm{sn}(z|k^2)$ from Abramowitz & Stegun (1965), $\epsilon$ is obtained as a function of $p$, namely $\epsilon = \mathrm{sn}\left(pw\sqrt{\lambda_1} \pm \Pi_0 | \frac{\lambda_1-\lambda_2}{\lambda_1}\right)$, with

$$\Pi_0 = \left| \mathrm{sn}^{-1}\left( \epsilon(r_{\mathrm{initial}}) | \frac{\lambda_1 - \lambda_2}{\lambda_1} \right) \right|. \tag{3.35}$$

Solving Eq. (3.33) for $r$ yields

$$r_{\pm}(p) = u + \frac{-2u \pm w(\lambda_1-\lambda_2)\mathrm{sn}\left(pw\sqrt{\lambda_1} \pm \Pi_0 | \frac{\lambda_1-\lambda_2}{\lambda_1}\right) \left| \mathrm{cn}\left(pw\sqrt{\lambda_1} \pm \Pi_0 | \frac{\lambda_1-\lambda_2}{\lambda_1}\right) \right|}{(\lambda_1-\lambda_2)\mathrm{sn}^2\left(pw\sqrt{\lambda_1} \pm \Pi_0 | \frac{\lambda_1-\lambda_2}{\lambda_1}\right) - (\lambda_1 - 1)}. \tag{3.36}$$

The case distinction denoted by the $\pm$ refers to the initial momentum in $r$ direction being positive ($p_r > 0 \rightarrow$ '+') or negative ($p_r < 0 \rightarrow$ '$-$'). In the case that $p_r = 0$, the initial position represents a turning point in $r$-coordinate and thus a root of $V_r$, as can be seen from the discussion in Sec. 3.2.1. Therefore the transform into Weierstrass' elliptic integral discussed in Sec. 3.2.2 can be used.

With this calculation, the coordinates $r$ and $\theta$ have been expressed as functions of $p$. The remaining coordinates can now simply be expressed by the parameter $p$ by using $r(p)$ and $\theta(p)$ in Eq. (2.44) and (2.45). The interested reader is referred to Yang & Wang (2013) for more details.

### 3.2.3. Carlson's Elliptical Integrals

Now that the coordinates $r, t, \theta, \phi$ and the affine parameter $\sigma$ have been expressed as functions of the new parameter $p$, it is clear from the previous section that many elliptical integrals need to be calculated. Following Yang & Wang (2013), crucial elliptic integrals are reduced into standard forms and subsequently evaluated by Carlson's method as presented by Dexter & Agol (2009).

Firstly, the standard forms

$$J_k(h) = \int_{x_1}^{x_2} \frac{\mathrm{d}x}{(x-h)^k \sqrt{4x^3 - d_2 x - d_3}} \tag{3.37}$$

$$I_k(h) = \int_{x_1}^{x^2} \frac{\mathrm{d}x}{(x-h)^k \sqrt{(x^2 - 2ux + u^2 + w^2)(x^2 + 2ux + u^2 + w^2)}}, \tag{3.38}$$

with constants $d_2, d_3, u$ and $w$ and $k \in \mathbb{Z}$ are introduced. From this, Eq. (2.42), Eq. (2.38) and Eq. (3.17), it follows that

$$J_0(h) = J_0 = \int_{x_1}^{x_2} \frac{\mathrm{d}x}{\sqrt{4x^3 - d_2 x - d_3}} \tag{3.39}$$

will be of importance. If $V_r$ has a real root, then from the discussion in Sec. 3.2.2 it is straight forward to see that the left side of Eq. (2.42) takes the form $J_0$ with $d_2 = h_2$ and $d_3 = h_3$. The same goes for the right side of Eq. (2.42), seeing from Sec. 3.2.2 it takes the form $J_0$ for $d_2 = g_2$ and $d_3 = g_3$. Thus together with Eq. (3.15), this becomes $p = J_0$. The remaining integrals in the equations of motion (Eq. 2.43,2.44 and 2.45) may be reduced to standard form in a similar fashion.

The radial integral of Eq. (2.43) can be reduced to

$$\sigma_r = \frac{{c_0}^2}{16} J_2\left(\frac{c_1}{4}\right) + \frac{c_0 r_{\mathrm{tp1}}}{2} J_1\left(\frac{c_1}{4}\right) + {r_{\mathrm{tp1}}}^2 J_0 \tag{3.40}$$

The radial integral of Eq. (2.44) can be expressed as

$$t_r = \sigma_r + \frac{c_0}{2} J_1\left(\frac{c_1}{4}\right) + (2r_{\mathrm{tp1}} + 4 + A_{t_+} - A_{t_-})p - B_{t_+} J_1(t_+) + B_{t_-} J_1(t_-), \tag{3.41}$$

where

$$\begin{aligned} r_\pm &= 1 \pm \sqrt{1 - a^2} \\ A_{t_\pm} &= \frac{2\left(r_\pm(4 - a\lambda) - 2a^2\right)}{(r_+ - r_-)(r_{\mathrm{tp1}} - r_\pm)} \\ B_{t_\pm} &= \frac{\left(r_\pm(4 - a\lambda) - 2a^2\right) c_0}{2(r_+ - r_-)(r_{\mathrm{tp1}} - r_\pm)^2} \\ t_\pm &= \frac{c_1}{4} \pm \frac{c_0}{4(r_\pm - r_{\mathrm{tp1}})}. \end{aligned} \tag{3.42}$$

The radial integral in Eq. (2.45) can be brought to the form

$$\phi_r = a\left(\left(A_{\phi_+} - A_{\phi_-}\right) J_0 - B_{\phi_+} J_1(t_+) + B_{\phi_-} J_1(t_-)\right), \tag{3.43}$$

where

$$\begin{aligned} A_{\phi_\pm} &= \frac{2r_\pm - a\lambda}{(r_+ - r_-)(r_{\mathrm{tp1}} - r_\pm)} \\ B_{\phi_\pm} &= \frac{(2r_\pm - a_\lambda)c_0}{4(r_+ - r_-)(r_{\mathrm{tp1}} - r_\pm)^2}. \end{aligned} \tag{3.44}$$

Therefore, for the case that $V_r$ has a real root, only the standard forms $J_0, J_1$ and $J_2$ are needed. However, as discussed before, the situation gets a bit more complicated if $V_r$ has

no real roots. Then the standard forms $I_k(h)$ are involved.

Following again Yang & Wang (2013) for the case that $V_r$ has no real roots, the radial integrals of Eq. (2.43)-(2.45) can be expressed as

$$\sigma_r = I_{-2}(0) \tag{3.45}$$
$$t_r = \sigma_r + 4J_0 + 2I_{-1}(0) + C_{t_+} I_1(r_+) - C_{t_-} I_1(r_-) \tag{3.46}$$
$$\phi_r = a\left(C_{\phi_+} I_1(r_+) - C_{\phi_-} I_1(r_-)\right), \tag{3.47}$$

with

$$C_{t_\pm} = \frac{2\left(r_\pm(4 - a\lambda) - 2a^2\right)}{r_+ - r_-}; \qquad C_{\phi_\pm} = \frac{2r_\pm - a\lambda}{r_+ - r_-}. \tag{3.48}$$

Thus all the radial integrals in the equations of motion Eq. (2.42)-(2.45) are reduced to the standard forms. What remains is the treatment of the $\theta$-, or equivalently the $\mu$-integrals.

Since the dependence of Eq. (2.44) on $\mu$ is the same as for Eq. (2.43), what remains is the reduction of the $\mu$-integrals in the expression for $\sigma$, i.e. Eq. (2.43) and in the expression for $\phi$, i.e. Eq. (2.45). This is readily done by Yang & Wang (2013) and results in

$$\sigma_\mu = t_\mu = a^2\left(\frac{{b_0}^2}{16} J_2\left(\frac{b_1}{4}\right) + \frac{b_0 \mu_{\mathrm{tp1}}}{2} J_1\left(\frac{b_1}{4}\right) + {\mu_{\mathrm{tp1}}}^2 J_0\right) \tag{3.49}$$

and

$$\phi_\mu = \lambda\left(\frac{J_0}{1 - {\mu_{\mathrm{tp1}}}^2} + W_{\mu_+} J_1(t_+) - W_{\mu_-} J_1(t_-)\right), \tag{3.50}$$

where

$$W_{\mu_\pm} = \frac{b_0}{8(\pm\mu_{\mathrm{tp1}} - 1)^2} \tag{3.51}$$
$$t_\pm = \frac{b_1}{4} + \frac{b_0}{4(-1 \pm \mu_{\mathrm{tp1}})}. \tag{3.52}$$

Thus in conclusion the simple looking expressions

$$\sigma = \sigma_r + \sigma_\mu \tag{3.53}$$
$$t = t_r + t_\mu \tag{3.54}$$
$$\phi = \phi_r + \phi_\mu \tag{3.55}$$

are found, in which every single expression is determined by the standard forms $J_k$ and $I_k$ defined in Eq. (3.37) and Eq. (3.38). The remaining task thus becomes calculating the integrals of these standard forms. This is done using Carlson's method.

If the polynomial $4x^3 - d_2 x - d_3$ has three roots $e_1, e_2, e_3$, Carlson (1988) showed that $J_k(h)$ takes the form

$$\begin{aligned} J_k(h) &= s_h \frac{1}{2} \int_z^y \frac{\mathrm{d}x}{\sqrt{(x-e_1)(x-e_2)(x-e_3)(x-h)^{2k}}} \\ &= s_h \frac{1}{2} \left[-1,-1,-1,-2k\right], \end{aligned} \tag{3.56}$$

where $s_h = \operatorname{sign}\left((z-h)^k\right)$ and Carlson's symbol $[p_1, \ldots, p_k]$ is defined as

$$[p_1, \ldots, p_k] := \int_z^y \prod_{i=1}^{k} (a_i + b_i t)^{p_i/2} \, \mathrm{d}t. \tag{3.57}$$

The study of these elliptic integrals was intensively done by Carlson (1988, 1989, 1991, 1992), who give formulae for the explicit calculation of integrals of the form Eq. (3.57). This takes care of the $J_k$. What remains is the treatment of the $I_k$, which are necessary in the case that $V_r$ has no real roots. As Carlson (1992) showed, the $I_k$ integrals reduce in a similar fashion to

$$\begin{aligned} I_k(h) &= s_h \int_z^y \frac{\mathrm{d}r}{\sqrt{(r^2 - 2ur + u^2 + w^2)(r^2 + 2ur + u^2 + v^2)(r-h)^{2k}}} \\ &= s_h \left[-1,-1,-1,-1,-2k\right], \end{aligned} \tag{3.58}$$

where $s_h$ and $[p_1, \ldots, p_k]$ have the same meaning as in Eq. (3.56).

Summarizing, in Sec. 3.2.2 the coordinates and thus equations of motion Eq. (2.42)-(2.45) were expressed as functions of the parameter $p$. This was done solely by using the knowledge about turning points of the geodesic (see Sec. 3.2.1) – that is the roots of $V_r$ and $V_\theta$ – as well as the constants of motion $\lambda$ and $q$ and initial coordinates and momenta. The resulting functions were composed of Weierstrass' and Jacobi's elliptic integrals which lead to the investigation of a convenient way to calculate those integrals. In Sec. 3.2.3, the coordinates as functions of $p$ were rewritten as combinations of standard elliptic integrals $J_k$ and $I_k$ defined in Eq. (3.37) and (3.38) which can readily be solved by Carlsons method, described by Carlson (1988, 1989, 1991, 1992). The calculation of the integrals is thus no longer an issue. The determination of the turning points $r_{\mathrm{tp}}$ and $\mu_{\mathrm{tp}}$ is a matter of root finding and several algorithms for finding the root of a quartic polynomial already exist. The only other information that entered the process described above that is not directly given as initial data, are the motion constants $\lambda$ and $q$. In order to solve the equations of motion completely, it is thus essential to extract the equations of motion from the initial data.

### 3.2.4. Constants of Motion as Function of $p$

First we may choose a chart in which the equations take a conveniently 'simple' form. Specifically here, the locally non-rotating observers will provide the desired charts. If

the initial conditions are given with respect to any other kind of reference frame, the components with respect to a locally non-rotating observer at that point can readily be calculated by a general Lorentz transformation.
Following Bardeen et al. (1972), the locally non-rotating frame (LNRF) is constructed by the basis vectors

$$e_{(a)}(\text{LNRF}) = e^{\nu}_{(a)}\partial_{\nu}, \tag{3.59}$$

where

$$e^{\nu}_{(a)} = \begin{pmatrix} e^{-\nu} & 0 & 0 & \omega e^{-\nu} \\ 0 & e^{-\mu_2} & 0 & 0 \\ 0 & 0 & e^{-\mu_3} & \\ 0 & 0 & 0 & e^{-\psi} \end{pmatrix}. \tag{3.60}$$

Note that this definition of the frame vectors is identical – up to order of the coordinates – to the definition of frame vectors of Eq. (2.22) in Sec. 2.2, which we identified as representing an inertial frame. Due to convention, the order used in Sec. 2.1 was $(t, \phi, r, \theta)$, whereas now the order is $(t, r, \theta, \phi)$. Seeing this resemblance to the frame vectors discussed before, this choice of vectors here indeed constitutes a frame and the property

$$e^{i}_{(a)} e_{(b)i} = \eta_{(a)(b)} \tag{3.61}$$

is in conformity with the notion of a locally non-rotating observer. Again, as in Sec. 2.2 the bracketed indices denote coordinates of the tetrad frame, whereas non-bracketed indices denote chart coordinates, more specifically the Boyer-Lindquist coordinates (Boyer & Lindquist 1967). The constants of motion will take a convenient form if expressed by the initial momenta with respect to the locally non-rotating frame. This shall suffice as reason to introduce the frame here once again, which is completely equivalent to any other reference frame.

Now, in accordance to the Hamiltonian Eq. (2.34), (2.35) and (2.42)- (2.45), the components of the four-momentum of a photon can be expressed in Boyer-Lindquist coordinates as

$$p_{\mu} = E\left(-1, s_r \frac{\sqrt{V_r}}{\Delta}, s_{\theta}\sqrt{V_{\theta}}, \lambda\right), \tag{3.62}$$

where $s_r$ and $s_{\theta}$ are the signs of the $r$- and the $\theta$-component respectively. Since these are components of a covector, they can readily be transformed into components with respect to the trad frame by

$$\bar{p}_{(a)} = e^{\mu}_{(a)} p_{\mu}, \tag{3.63}$$

where $\bar{p}_{(a)}$ are the components of the four-momentum with respect to a locally non-rotating frame, $p_{\mu}$ are the components in the Boyer-Lindquist coordinates and $e^{\mu}_{(a)}$ are as

defined in Eq. (3.60). Thus (see Shakura 1987)

$$\bar{p}_{(t)} = -Ee^{-\nu}\left(1-\lambda\omega\right) \tag{3.64}$$

$$\bar{p}_{(r)} = s_r Ee^{-\mu_2}\frac{\sqrt{V_r}}{\Delta} \tag{3.65}$$

$$\bar{p}_{(\theta)} = s_\theta Ee^{-\mu_3}\sqrt{V_\theta} \tag{3.66}$$

$$\bar{p}_{(\phi)} = E\lambda e^{\psi}. \tag{3.67}$$

From Eq. (3.64) and (3.67), $\lambda$ can be determined as

$$\lambda = \frac{\sin(\theta)\frac{\bar{p}_{(\phi)}}{\bar{p}_{(t)}}}{-\Sigma\frac{\sqrt{\Delta}}{\rho^2}+\omega\sin(\theta)\frac{\bar{p}_{(\phi)}}{\bar{p}_{(t)}}}. \tag{3.68}$$

Eq. (3.64) also yields

$$E = -\frac{\bar{p}_{(t)}e^{\nu}}{(1-\lambda\omega)} \tag{3.69}$$

Inserting the result for $E$ and $\lambda$ into Eq. (3.66), the constant of motion $q$ can be expressed as

$$q = \left[\left(\frac{\frac{\bar{p}_{(\phi)}}{\bar{p}_{(t)}}}{-\Sigma\frac{\sqrt{\Delta}}{\rho^2}+\omega\sin(\theta)\frac{\bar{p}_{(\phi)}}{\bar{p}_{(t)}}}\right)^2 - a^2\right]\cos^2(\theta) + \left[\frac{\bar{p}_{(\theta)}}{\bar{p}_{(t)}}(1-\lambda\omega)\right]^2\frac{\rho^2}{\Delta} \tag{3.70}$$

Thus the motion constants can be calculated from the components of the four-momentum $\bar{p}_{(a)}$ with respect to the LNRF. However, the components of the four-momentum may not be given with respect to the LNRF, but to some other choice of frame. It is convenient to use a general Lorentz transformation from that choice of frame into the LNRF and continue the calculations with these components.

Considering a reference frame with physical velocities $v_r, v_\theta, v_\phi$ with respect to the LNRF. The two systems of reference are connected by $\bar{p}_{(a)} = \alpha_a^{(b)}p'_{(b)}$, where $\bar{p}_{(a)}$ are the components of the four-momentum in the LNRF and $p'_{(b)}$ are the components of the four-momentum in the reference frame of choice. The term $\alpha_a^{(b)}$ connecting the two is the Lorentz matrix given by (Misner et al. 1973)

$$\alpha_a^{(b)} = \begin{pmatrix} \gamma & -\gamma v_r & -\gamma v_\theta & -\gamma v_\phi \\ -\gamma v_r & 1+\frac{\gamma^2 {v_r}^2}{1+\gamma} & \frac{\gamma^2 v_r v_\theta}{1+\gamma} & \frac{\gamma^2 v_r v_\phi}{(1+\gamma)} \\ -\gamma v_\theta & \frac{\gamma^2 v_r v_\theta}{(1+\gamma)} & 1+\frac{\gamma^2 {v_\theta}^2}{(1+\gamma)} & \frac{\gamma^2 v_\theta v_\phi}{(1+\gamma)} \\ -\gamma v_\phi & \frac{\gamma^2 v_r v_\phi}{(1+\gamma)} & \frac{\gamma^2 v_\theta v_\phi}{(1+\gamma^2} & 1+\frac{\gamma^2 {v_\phi}^2}{(1+\gamma)} \end{pmatrix}. \tag{3.71}$$

With this in mind the crucial quotient $\frac{\bar{p}_{(a)}}{\bar{p}_{(t)}}$ appearing in Eq. (3.68) and (3.70) can be expressed from the components of the four-momenta with respect to another frame as

$$\frac{\bar{p}_{(a)}}{\bar{p}_{(t)}} = \frac{\alpha_a^{(t)}+\alpha_a^{(\alpha)}\frac{p'_{(\alpha)}}{\bar{p}'_{(t)}}}{\alpha_t^{(t)}+\alpha_t^{(\alpha)}\frac{p'_{(\alpha)}}{p'_t}}. \tag{3.72}$$

This concludes the technical treatment of the solution of the equations of motion. The geodesics can now be calculated, once the initial position and the initial four-momentum of the photon is provided. The remaining task is to derive the physical quantities from these considerations, which in turn permit the calculation of the intensity profile on the disk. Next to geometrical considerations like the proper area and the Lorentz factor of the disk, which remain as in Sec. 3.1, a formula for the energy shift in the general case is necessary.

### 3.2.5. Energy Shift

The energy shift a photon undergoes on its way from the emitter to the accretion disk is defined as the ratio

$$g = \frac{E_{\text{obs}}}{E_{\text{em}}}, \tag{3.73}$$

where $E_{\text{obs}}$ is the energy of the photon measured by the observer (the disk) and $E_{\text{em}}$ is the energy of the photon measured by the emitter. Thus it is clear that $E_{\text{em}} = -p'_{(t)}$ and $E_{\text{obs}} = -p_a \, {u_{\text{obs}}}^a$, where ${u_{\text{em}}}^\mu$ is the four-velocity of the emitter.

To get a concise notation, we define

$$f_t := \frac{\bar{p}_{(t)}}{p'_{(t)}} = \alpha_t^{(t)} + \alpha_t^{(i)} \frac{p'_{(i)}}{p'_{(t)}}, \tag{3.74}$$

where $p'_{(t)}$ is the $t$-component of the four-momentum in the emitters frame of reference and $\bar{p}_{(t)}$ is the $t$-component of the four momentum with respect to the LNRF. Using this definition with Eq. (3.64), we find

$$E_{\text{em}} = -p'_{(t)} = \bar{p}_{(t)} \frac{p'_{(t)}}{\bar{p}_{(t)}} = E e^{-\nu} (1 - \lambda\omega) \frac{1}{f_t}. \tag{3.75}$$

This provides a formula to evaluate the denominator of Eq. (3.73) from the initial momentum $p'$.

It remains to find such an expression for the numerator. Using knowledge about the special form of the disk velocity given in Eq. (2.51) quickly leads to the desired expression. However, cases in which the disk velocity is modified due to physical circumstances may be interesting as well. So keeping ${u_{\text{obs}}}^a$ unrestricted gains the possibility of modifying the disk motion later on and indeed does not cause too much extra effort. The simplification to the standard disk model will then come as a simple reduction of the general formula. May the coordinate velocities be ${u_{\text{obs}}}^a = \frac{\mathrm{d}x^a}{\mathrm{d}\tau} \left(u^t, u^r, u^\theta, u^\phi\right)$ with $\tau$ being the observer's proper time. Then from Eq. (3.62) the energy of the photon measured by the observer

can be expressed as

$$E_{\rm obs} = E\left(u^t + s_r\frac{\sqrt{V_r}}{\Delta}u^r + s_\theta\sqrt{V_\theta}u^\theta + \lambda u^\phi\right) \tag{3.76}$$

$$= Eu^t\left(1 + s_r\frac{\sqrt{V_r}}{\Delta}\frac{{\rm d}r}{{\rm d}t} + s_\theta\sqrt{V_\theta}\frac{{\rm d}\theta}{{\rm d}t} + \lambda\frac{{\rm d}\phi}{{\rm d}t}\right). \tag{3.77}$$

Then the general formula for the energy shift a photon undergoes from the emitter to an observer can be written as

$$g = \frac{E_{\rm obs}}{E_{\rm em}} = \frac{\left(u^t + s_r u^r\frac{\sqrt{V_r}}{\Delta} + s_\theta u^\theta\sqrt{V_\theta} + \lambda u^\phi\right)\Big|_{\rm obs}}{\left(e^{-\nu}(1-\lambda\omega)\frac{1}{f_t}\right)\Big|_{\rm em}} \tag{3.78}$$

$$= \frac{\left(u^t\left(1 + s_r\frac{{\rm d}r}{{\rm d}t}\frac{\sqrt{V_r}}{\Delta} + s_\theta\frac{{\rm d}\theta}{{\rm d}t}\sqrt{V_\theta} - \lambda\frac{{\rm d}\phi}{{\rm d}t}\right)\right)\Big|_{\rm obs}}{\left(e^{-\nu}(1-\lambda\omega)\frac{1}{f_t}\right)\Big|_{\rm em}}, \tag{3.79}$$

where $(\dots)\big|_{\rm obs/em}$ means that the terms appearing in the brackets are to be evaluated at the position of the observer/emitter respectively. The disk was assumed to exhibit circular motion in the equatorial plane, that is $u^r_{\rm disk} = \frac{{\rm d}r}{{\rm d}t} = u^\theta_{\rm disk} = \frac{{\rm d}\theta}{{\rm d}t} = 0$. For such an accretion disk the energy shift amounts to

$$g_{\rm equat,circ} = \frac{u^t_{\rm disk}\left(1-\Omega\lambda\right)\Big|_{\rm obs}}{\left(e^{-\nu}(1-\lambda\omega)\frac{1}{f_t}\right)\Big|_{\rm em}}. \tag{3.80}$$

Indeed, for the case of the lamp post model, i.e. an emitter on the rotational axis ($\lambda = 0$) and the standard accretion disk as the observer ($u^t_{\rm disk}$ as in Eq. 2.53), the formula for the energy shift reduces down to the 'lamp post formula for the energy shift' derived in Chapt. 3.1. As such, Eq. (3.79) is the generalization of the formula presented in the theory of the lamp post model.

In summary, in this chapter, the equations of motion have been reduced to elliptical integrals in a standard form and solving them has become a mere problem of root finding and application of Carlson's method. The evaluation of these integrals in this form is much faster than direct Legendre quadrature of the general equations (2.42) (2.45) and the root finding process can be done using the Newton-Raphson procedure or a bisection method. The energy shift formula (Eq. 3.79) found in this section now enables us to generalize the calculation of the intensity profile from a general emitter in the vicinity of a black hole. From the above, it is clear that all the tools to calculate the intensity

profile of a point source are assembled. Owing to the fact that the incident energy is an additive quantity, the intensity profile of an extended source may then be approximated by the sum of the intensities of multiple point sources. This method trivially extends to extended source of any type of geometry, exhibiting motion of constant velocity. In the following chapter, the intensity profiles for the lamp post geometry calculated by Dauser (2010) and calculated from this code are compared. Once the validity of the method is supported by this comparison, the intensity profile for off-axis and extended sources will be compared to other works, namely Wilkins & Fabian (2012).

# 4. Illumination of the Accretion Disk

## 4.1. Implementation

The previously discussed theory allows us to calculate calculation of the intensity profile on the accretion disk from apoint source at a given location in spacetime. This section serves as a short introduction to the code developed by this thesis. The code simulates an isotropically emitting point source at height specified height $h$ and distance $x$ from the rotational axis and calculates the incident intensity on the accretion disk of a black hole with given spin parameter $a$ due to this source. To do so, the radii at which the simulated photons hit the accretion disk are calculated in a first step and this information is then further converted into the incident intensity in a second step. Unless further specified, the data for the figures in the following sections 4.2 and 4.3 was produced using this code.

To calculate the incident radii of the simulated photons on the disk, the code requires the user to provide information about the black hole spin parameter $a$, the coordinates $r$ and $\theta$ of the source's location in the Boyer-Lindquist system and the number of photons $N$ that the code is supposed to simulate. The information about the source's location in terms of the height $h$ above the black hole/accretion disk and the distance $x$ to the axis of symmetry may be calculated from the given coordinates $r$ and $\theta$ as

$$x = \sqrt{r^2 + a^2}\sin(\theta) \tag{4.1}$$

$$h = r\cos(\theta). \tag{4.2}$$

Conversely, if the user was to simulate the emission for a source at given height $h$ and $x$, the equation

$$x = \sqrt{h^2\tan(\theta)^2 + a^2\sin(\theta)^2} \tag{4.3}$$

has to be solved for $\theta$ and $r$ is then obtained as

$$r = \frac{h}{\cos(\theta)}. \tag{4.4}$$

The user then provides the code with the results for $r$ and $\theta$. Additionally, the algorithm is set up to also take information about where to store the calculated data from the input file.

To uniquely characterize the emitting source, the source's velocity has to be specified as well. As it is difficult to provide meaningful velocity models for the source via an input file, the information about the source's velocity is given in the code itself. To change the velocity model of the source, the code itself has to be altered.

The velocity model used in the further sections assumes that the source is co-rotating with the accretions disk element at the same distance to the axis of symmetry. The reasoning behind this model is that any source with a finite distance to the axis of symmetry must have an angular velocity as to sustain this distance and not fall onto the rotational axis. For sources close to the accretion disk, the co-rotation model serves

as an approximation of the required angular velocity for circular orbits. If the X-ray source originates from the magnetic reconnection in poloidal field lines emerging from the ionized accretion disk, the emitting source is also expected to move along the rotating disk (see Wilkins & Fabian, 2012). This velocity model was also chosen in calculations of Wilkins & Fabian (2012) for off-axis sources and therefore it comes with the advantage of having a set of reference data provided by these previous calculations. In the case of a lamp post source, the velocity model reduces to a stationary point source.

Now, given the above mentioned information, the output of the program is a file, containing the incident radii, initial azimuthal and polar emission angles, the initial momenta and the constants of motion $\lambda$ and $q$ of the simulated photon. Additionally, the code echoes back the information about the source into the output file, so that all necessary information for further analysis of the data is gathered in a single file. The post processing of the output file into an intensity and photon flux profile is done via a separate script in python.

Once the information about the source is loaded into the code, the velocity of the source for that location is calculated as

$$v^\mu = (v^r, v^\theta, v^\phi) = (0, 0, v^\phi) \qquad \text{with} \tag{4.5}$$

$$v^\phi = e^{\psi-\nu}\left(\frac{1}{\left(\sqrt{r^2+a^2}\sin(\theta)\right)^{3/2}} - \omega\right) \tag{4.6}$$

which is just the aforementioned model of co-rotation with the disk element at distance $\sqrt{r^2+a^2}\sin(\theta)$ from the black hole. Following the determined angular velocity, the emission angles of the photons are determined. To this end, an azimuthal emission angle $\phi_{\text{in}}$ is drawn from a uniform random distribution in the range of $[0, 2\pi]$ and a polar angle $\theta_{\text{in}}$ is calculated from a further random number $y$ – drawn from a uniform random distribution – as

$$\theta_{\text{in}} = \arccos(1-2y). \tag{4.7}$$

These two distributions come from the fact that the solid angle element at an angle $\theta$ is given by

$$\mathrm{d}A = \sin(\theta)\mathrm{d}\phi\,\mathrm{d}\theta \tag{4.8}$$

and then using inverse transform sampling on this (Kolonko 2008) .
By choosing this Monte Carlo approach of determining the emission angles, we make sure that no systematic effects are introduced from the specific choice of emission angles. An example for such systematic effects arises from the axisymmetry of Kerr spacetime. Two photons that are emitted under the same $\theta_{\text{in}}$ in the lamp post geometry are bound to arrive at the same incident radius on the disk. Were the emission angles given for example as fixed, equally spaced angles, the photons would bunch to discrete incident radii. In the case of the lamp post geometry, this problem can indeed be avoided while still maintaining fixed emission angles (as done by Dauser, 2014), however such systematic

effects arise in a more complex form for off-axis sources. We therefore avoid possible systematic effects by using this Monte Carlo approach, at the cost of possible longer computational time to achieve a representative sampling.
Once the code has established the emission angles, it calculates the parameter $p_{\mathrm{inc}}$, already used in the previous chapter, for which $\theta(p) = \pi/2$. This is done using the function *pemfind* of the *YNOGK*-code of Yang & Wang (2013). The remaining coordinates $r_{\mathrm{inc}} = r(p_{\mathrm{inc}})$ and $\phi_{\mathrm{inc}} = \phi(p_{\mathrm{inc}})$ are then calculated by the *ynogk* function again provided in the likewise named code by Yang & Wang (2013). Lastly, the above initially mentioned information is written into a data file from which the incident photon- and intensity flux can be calculated.

The results shown in the following sections were created using simulations of $10^8$ photons for each combination of initial parameters. Each of these simulations had a runtime of between 20-30 minutes on a standard desktop computer with an Intel Core i7 7700 (QuadCore), 3.6 GHz processor.

## 4.2. The Lamp Post Model

The functionality of the code can be tested best on the simpler case of the lamp post geometry. With all of the effects discussed in Chap. 3 taken into account it is possible to calculate the intensity profile on the surface of the accretion disk caused by a source on the rotational axis of the black hole. As mentioned before, the emission from a stationary point source on the axis of symmetry is determined by the location of the source and the emission angle $\delta$. It is therefore sufficient to provide the coordinates of the source and an emission model to derive the corresponding intensity profile on the disk. Although it is possible to consider anisotropic emitters, at this point there is no reason to artificially distinguish a certain direction. Hence in the following, a stationary, isotropic source will be modeled.

The photon flux $I$ can be calculated as

$$I = \frac{N_{\mathrm{Photo}}(r, \Delta r)}{2\pi r \Delta r}, \tag{4.9}$$

with $N_{\mathrm{Photo}}(r, \Delta r)$ being the number of photons incident in a radius interval of width $\Delta r$ centered around the radius $r$. This number of photons is determined by the incident radii – calculated by using the methods described in Sec. 3.1 – and the area $2\pi r \Delta r$ of a radial bin, which is calculated as the area of an annulus of radius $r$, with width $\Delta r$ in euclidean space. The result for varying source heights $h$ and spin parameters $a$ are depicted in Fig. 4.1 and Fig. 4.2. Figure 4.1 clearly shows that the biggest influence of the spin parameter $a$ is the determination of the inner edge of the disk. The photon fluxes for different parameters $a$ are close to identical to each other. The main difference being that for large positive spin parameter $a$, the accretion disk extends further down towards the black hole and as such, photons are also incident at smaller radii. The maximum value for any parameter is always achieved at the innermost radius, which is expected, as the flux is expected to be largest close to its source. At large radii, far away from the

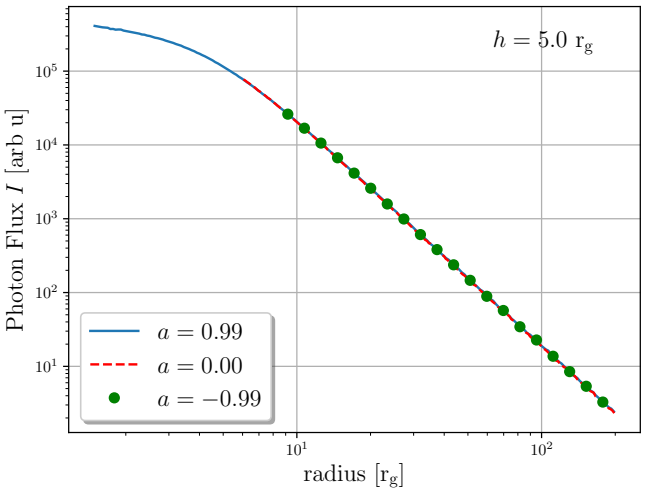


**Figure 4.1:** Photon flux on the disk generated by an isotropically emitting point source at height 5 $r_g$ and varying spin parameter $a$. As apparent from the figure, the biggest influence of the spin parameter on the photon flux profile is the determination of the innermost stable radius.

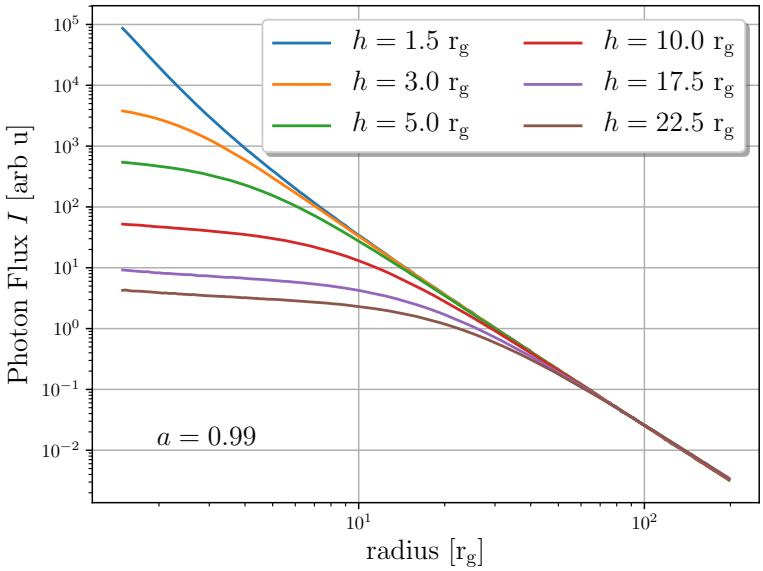


**Figure 4.2:** Photon flux on the disk generated by isotropically emitting point source at varying heights and a spin parameter $a = 0.99$. As apparent from the figure, the height influences the qualitative behavior of the photon flux.

black hole, the spectra resemble a power law directly proportional to $r^{-3}$.
The photon flux for different source heights $h$ can be seen in Fig. 4.2. From this, it is apparent that the height of the primary source influences the qualitative behavior of the photon flux profile. For large source heights, the profile remains shallow until $r_{\text{inc}} \approx h/2$, where it transitions into a power law shape like $r^{-3}$ again. For low emission heights, the profile steepens early and transitions into the same power law for large radii.

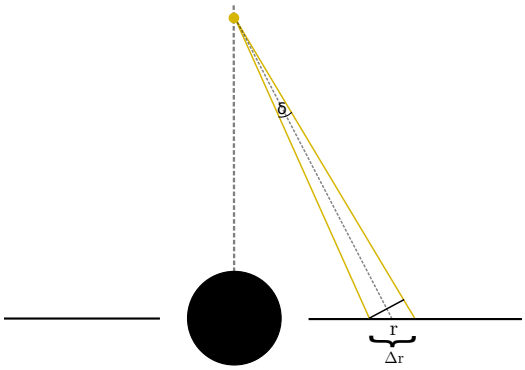


**Figure 4.3:** Sketch to visualize the geometric considerations that lead to Eq. 4.10.

To highlight the effect of gravity on the incident photon flux, the case of flat space, i.e. the absence of mass that would generate a gravitational field may be regarded as well. Since spacetime is then globally described by the Minkowski metric, that is, the spatial part is simply euclidean, the photon flux can be calculated analytically. From geometric considerations on Fig. 4.4, the incident flux in flat spacetime is obtained as (see also Dauser, 2014)

$$I_{\text{flat}}(r) = \frac{1}{A(r, \Delta r)} = \frac{\cos(\delta)}{(r^2 + h^2)} = \frac{h}{(r^2 + h^2)^{3/2}}. \tag{4.10}$$

As discussed in Sec. 2.1, the Kerr spacetime is asymptotically flat for $r \to \infty$. As such, the incident photon flux on the disk for any combination of the parameters $h, M$ and $a$ is expected to converge towards the theoretical photon flux in flat spacetime Eq. 4.10. For large radii $r$, the initial height of the source is negligible and as such, the statement above reduces to the expectation that the photon flux far away from the influence of the black hole follows a power law, with radial dependency of $I(r) \propto r^{-3}$. This is in agreement with the behavior of the fluxes in Fig. 4.2 and can clearly be seen in Fig. 4.4. On the inner regions of the accretion disk however, the effects of gravitation are significant, as the photon flux calculated for Kerr spacetime is noticeably higher than expected for flat spacetime. This increase in photon flux at the inner regions is readily explained by the light bending in the strong gravitational field of the black hole.

The obtained photon flux is consistent with the expectations. The maximal illumination is always reached closest to the source's location and at large radii, the flux profile approaches a constant power law, as expected in flat spacetime. As a final step, the results for the photon flux achieved in this thesis are compared to previous results. The photon flux presented in the work of Dauser et al. (2013) is used for reference.

Summarizing the investigation of the calculated photon flux, we find that the influence of the spin parameter $a$ expresses itself mostly by determining radius of the inner edge of the accretion disk. The emission height $h$ has qualitative influence on the flux profile, as

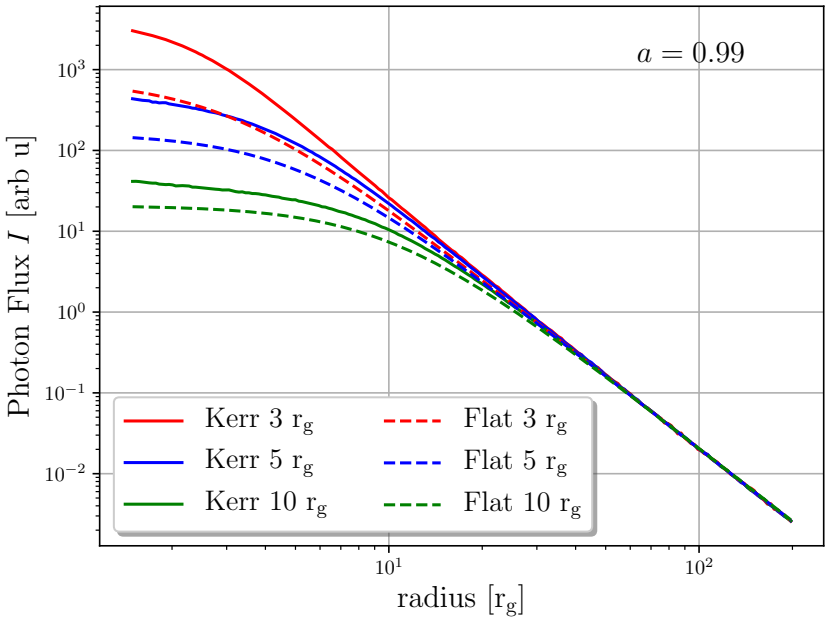


**Figure 4.4:** Photon flux $I$ of a point source on the rotational axis of the black hole for different emission heights and the respective photon fluxes in flat spacetime. The fluxes are normalized to match at large radii. The flux in Kerr spacetime at small radii is enhanced compared to flat spacetime due to gravitational light bending.

the profiles are shallow until $r_{\text{inc}} \approx h/2$ and then transition into a power law shape of $r^{-3}$ for large radii. The power law shape at large radii is in conformity with the asymptotical flatness of Kerr spacetime far away from the central object as the photon flux in euclidean spacetime follows the same shape (see Eq. 4.10).

The analysis of the incident photon flux on the accretion disk already gave great insight on the importance of the parameters $a$ and $h$ and their influence on the photon trajectories. The physically more interesting quantity however is the proper energy flux incident on the accretion disk. To determine this incident intensity, the proper area of a disk element, the accretion disk's Lorentz factor and the energy shift of the photons along their trajectory have to be taken into account. This can be done from the discussion of these effects in Sec. 3.1.1 and Sec. 3.1.2. Following Dauser et al. (2013), the intensity profile on the disk can be calculated as

$$F_{\text{i}}(r_{\text{i}}, h) = \Big[\sin(\delta)\Big] \frac{g^{\Gamma}}{A(r, \Delta r)\gamma^{(\phi)}}, \tag{4.11}$$

where $\Gamma$ is the photon index that arises from the power law shape of the emitted radiation. On average, sources showing relativistic reflection are observed to have a photon index of around $\Gamma = 2$ (see Walton et al., 2013; Fig. 1.3 upper panel). The factor $\sin(\theta)$ is

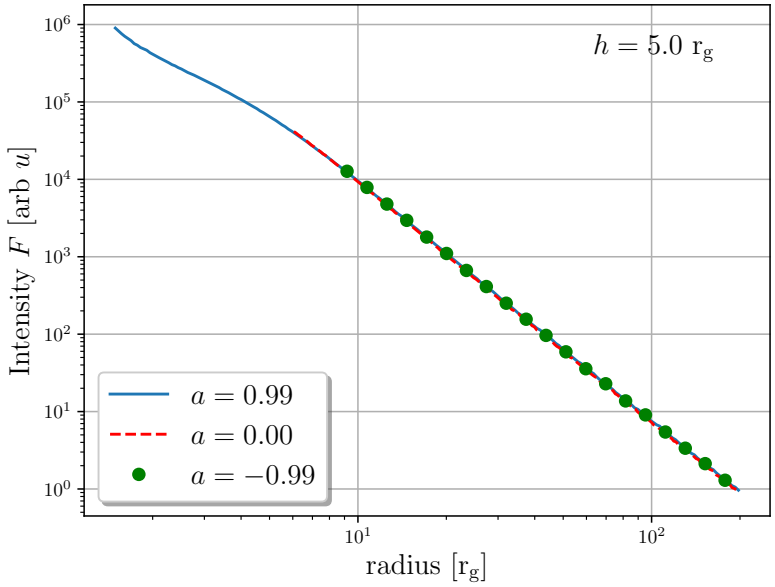


**Figure 4.5:** Intensity profile on the accretion disk, caused by a point source at emission height $h = 5\ r_g$ and varying spin parameters. Similarly to the photon flux, the biggest influence of the spin parameter on the intensity profile is the determination of the innermost radii of the accretion disk.

written in gray and encapsulated in brackets to denote the fact that in the work of Dauser (2014), the emission was modeled into equally spaced angles. The sine term corrects this model to an isotropic emission. In the calculations presented here, the source is already implemented as isotropic (see eq. 4.7) and the correction term is not needed. Note also that the photon flux is contained in the above formula in the area term in the denominator, since Dauser (2010) chose the binning of the photon flux in such a way that always one photon is counted per bin. This choice was not adapted for the sake of this thesis, as it would amplify the statistical noise caused by drawing the emission angles from a probability distribution. So the incident intensity is here calculated as

$$F_\mathrm{i}(r_\mathrm{i}, h) = \frac{g^\Gamma}{\gamma^\phi} \cdot \frac{N_\mathrm{Photon}(r_\mathrm{i}, \Delta r_\mathrm{i})}{A_\mathrm{Kerr}(r_\mathrm{i}, \Delta r_\mathrm{i})} = \frac{g^\Gamma}{\gamma^{(\phi)}} \cdot \frac{A_\mathrm{Flat}(r_\mathrm{i}, \Delta r_\mathrm{i})}{A_\mathrm{Kerr}(r_\mathrm{i}, \Delta r_\mathrm{i})} \cdot I(r_\mathrm{i}, \Delta r_\mathrm{i}). \tag{4.12}$$

The intensity profiles for varying spin parameters $a$ are depicted in Fig. 4.5 and for varying emission heights in Fig. 4.6. Similarly to the discussion of the photon flux, the dependence of the intensity profile on the spin parameter $a$ is limited to the determination of the inner edge of the accretion disk. Also analogous to the discussion of the photon flux, the profile is generally flattened until $r_\mathrm{inc} \approx h/2$ at which point the profile transitions into a power law shape. In the intensity profile however, a steep drop at the innermost radii can be seen for all emission heights. This steep drop can not be seen if the profile starts at large radii due to low spin parameters. This largely enhanced intensity towards small radii is explained by the energy shift of those photons. As displayed in Fig. 3.3, the energy shift enhances the intensity at low radii up to a factor of 100 and drops off very quickly towards the outer radii. The energy shift thus has a stronger influence on the intensity profile on the inner parts of the disk than the light bending effects that were displayed in Fig. 4.3.

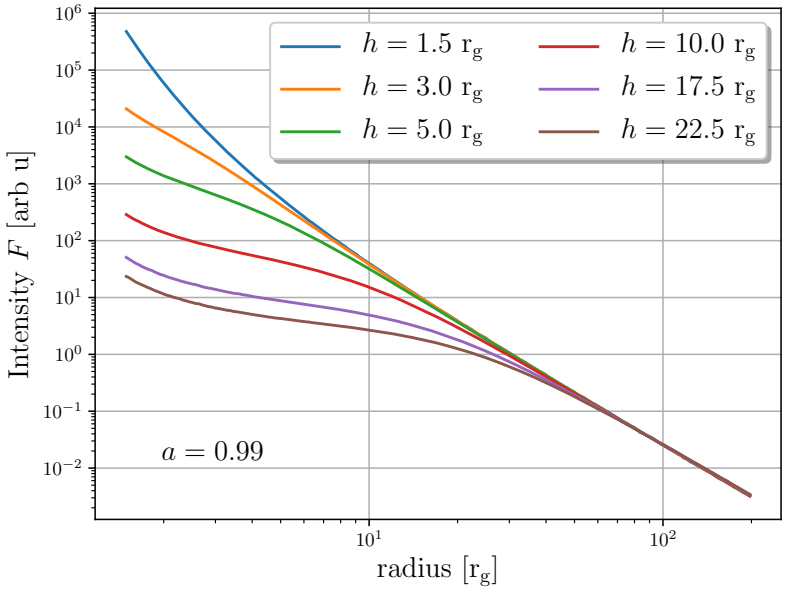


**Figure 4.6:** Intensity profile on the accretion disk caused by a point source of varying emission heights $h$ and a spin parameter $a = 0.99$. Similarly to the photon flux, the emission height $h$ has influence on the qualitative behaviour of the profile.

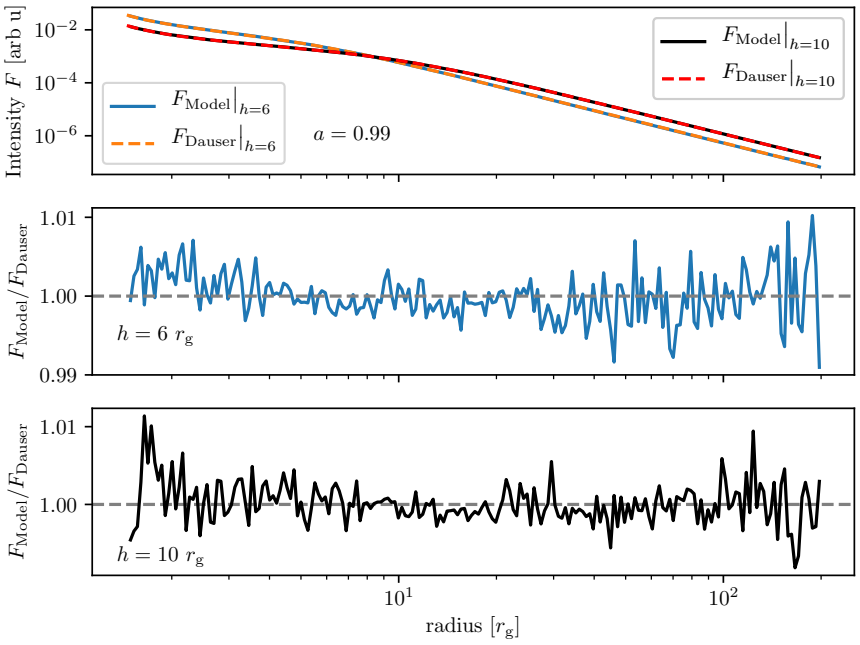


**Figure 4.7:** Example for a comparison of the calculated photon flux with fixed angular steps to the photon flux provided by the relxill model v1.3.3 for an isotropic point source at height 6 $r_g$ and 10 $r_g$ and a spin parameter of $a = 0.99$. The second panel shows the deviation from the reference data. The oscillation is attributed to statistical noise coming mainly from the random assignment of emission angles.

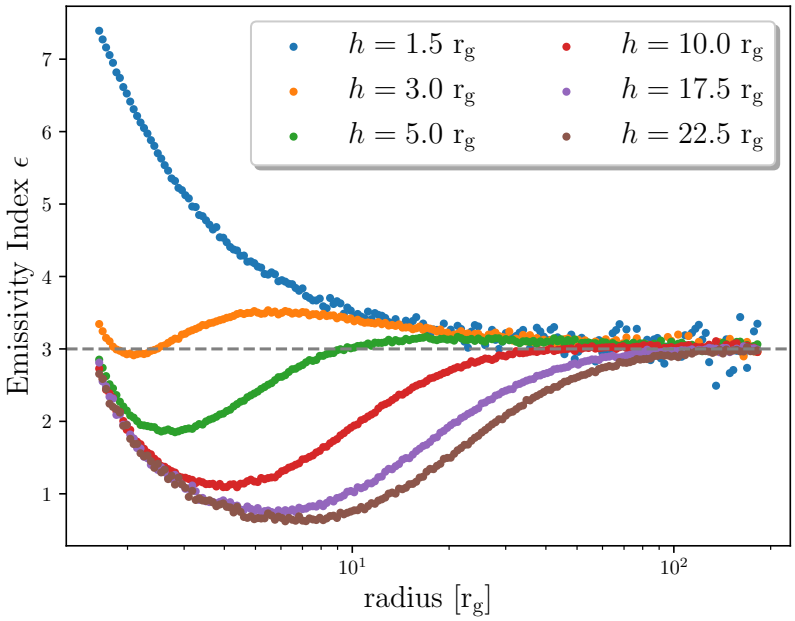


**Figure 4.8:** Emissivity Index $\epsilon$ for different emission heights $h$ and a spin parameter $a = 0.99$.

The result of Fig. 4.6 can be expressed in a form that is more easily connected to observations. The spectra that are actually measured from the vicinity of a black hole are usually energy spectra. To extract the radial distribution of intensity on the disk, a power law is modeled to the accretion disk and the contribution of several disk elements to the total spectrum is calculated. If the data is good enough, a single power law will prove to be a bad model for the illumination of the disk. As such, usually the power law index is free to vary for each modeled disk segment. Thus the physical quantity belonging to the illumination of the disk that can be fit to measured data is usually not the intensity itself, but the power law exponent that describes the illumination of each respective disk segment. The intensity profile may thus locally be expressed as a power law

$$F(r, h) \propto r^{-\epsilon}, \tag{4.13}$$

where the exponent $\epsilon$ is a measure for the steepness of the profile. For large radii, the intensity profile resembles a power law $F(r, h) \propto r^{-3}$, whereas the profile flattens at intermediate radii and steepens at small radii. In a double logarithmic presentation of the intensity profile, the emissivity index $\epsilon$ arises as the local slope of the profile. The emissivity index for different emission heights is depicted in Fig. 4.8. For each source height $h$, the profile of the emissivity index can be divided into three regions. Firstly, for large radii (i.e. $r \geq 2h$), the emissivity index approaches a constant value of 3 as expected in flat space. for intermediate radii, the emissivity profile first rises towards low radii, which may be attributed to gravitational light bending and the effect of the energy shift and towards smaller radii, this increase transitions into a drop off. At the innermost radii, below about $2\,r_g$, the profile is dominated by a strong steepening of the profile towards the inner radii. This steepening is explained by the effect of the

gravitational energy shift and in turn on the photon index $\Gamma$ of the primary photon source. Especially at large radii and low emission heights, statistical noise is visible in the emissivity index profile. This noise becomes dominant for large radii, as fewer photons arrive at large incident radii and thus the statistic is worse than at the inner regions. This is worst for sources at low emission heights, as even fewer photons reach large radii. Although this kind of statistical noise is already present in the profiles of the photon flux and the energy intensity, the emissivity index is extracted from those spectra via the slope, i.e. a derivative, of the data in double logarithmic presentation. Thus, even small fluctuations in the intensity data can appear as large variations in the emissivity index. The noise can be reduced by simulating more photons at cost of computational time or by computing the slope of the data over more data points. The latter however comes with the disadvantage of also moderating sudden changes in the profile that may not necessarily come from statistical noise. The high statistical noise in the undersampled regions may also be reduced by adapting the angular distribution of the simulated photons using some kind of statistical weight in such a way, that all regions are sampled fairly equally and correcting for the modified photon emission post simulation. This was however not done within the scope of this thesis.

Although the qualitative discussion of the photon flux-, intensity-, and emissivity index profile is in agreement with previous works on the lamp post geometry, a quantitative comparison is still necessary to confirm the validity of the results. The reference data was taken from the relxill model v1.3.3 (see García et al. 2014). An example comparison of the results to the reference data can be seen in Fig. 4.7 for a isotropic point sources located on the axis of symmetry at height $6\,r_\mathrm{g}$ and $10\,r_\mathrm{g}$ above a black hole with spin parameter $a = 0.99$. For closer investigation of the differences, the quotient of the calculated emission profile and the reference profile is depicted in the second panel of Fig. 4.7. Especially from the second panel, it is apparent that statistical noise dominates the deviation of the two spectra. The fluctuations decrease with increasing number of simulated photons and it is suspected that the calculated profile converges towards the reference profile. The comparison in Fig. 4.7 was created with the data of the simulation of $10^8$ photons and the spectrum differs from the reference data by less than 1.2%. Since the photon flux can be calculated by multiplication of the intensity profile with the correction factors for proper area, Lorentz boosting, and energy shift, the agreement of the intensity profiles also implicates agreement of the photon fluxes. Further, since the emissivity index profile is also extracted directly from the calculated intensities, the emissivity profile is expected to agree with the reference data quantitatively as well. As such, the model indeed reproduces the results of previous works on the lamp post geometry.

Overall, the energy shift $g$ and the spectral shape of the emitted photons that determines the photon index $\Gamma$ have the most influence on the profile at the innermost region of the accretion disk. At intermediate radii, the emission height is the determining parameter for the shape of the irradiation profile at intermediate radii. At large radii, all profiles transition towards a $r^{-3}$ power law as in flat spacetime.

## 4.3. The General Model

Since the results for the lamp post geometry were in agreement with previous works both qualitatively and quantitatively, the confidence in the presented code is sufficient to test it in the general case. The method of doing so will be similar to the testing in the lamp post geometry, i.e. we investigate the qualitative behavior of the photon flux and the intensity when changing the determining parameters and then compare the spectra to previous work for a quantitative assessment. In the lamp post case, there were two determining parameters: The spin parameter $a$ of the black hole and the height $h$ of the source above the black hole. For a general point source, the distance of the source to the rotational axis may also be varied. This leaves us with three variable parameters. Furthermore, the source may now also have an angular velocity around the axis of symmetry which can be modeled as well. In the following, a source at distance $x$ from the axis of symmetry is assumed to be co-rotating with the disk element at distance $x$ from the black hole, as mentioned in Sec. 4.1.

A point source with non-vanishing distance to the rotational axis breaks the otherwise symmetric geometry of the black hole system, as the irradiation on the disk will now also be dependent on the coordinate $\phi$. The results for such a point source are thus most conveniently displayed in a 2D representation. An example for emission by a co-rotating point source at height $h = 5\ r_{\mathrm{g}}$ and at distance $x = 5\ r_{\mathrm{g}}$ to the rotational axis at $\phi = 0$ can be found in Fig. 4.9 As expected, the illumination is not symmetric around the rotational axis. A region of high photon flux is visible close to the point of emission. The deviation of the center of this so called hotspot can be explained by two effects that have the same fundamental cause. First of all, the emission of the photons is focused in the direction of the current velocity of the source due to Lorentz boosting. In this case, as the source is moving in a circular counter clockwise orbit, the emission is focused in the negative $y$-direction. Therefore the hotspot is shifted to in polar coordinates towards negative $\phi$ values, whereas the source location is at $\phi = 0$. Secondly, the already discussed effect of frame dragging drags the emitted photons along a seemingly counter clockwise rotating trajectory, leading to a shift towards negative $\phi$ values (see 2.2). Increasing the source height results in the center of the hotspot being shifted even further away from the source's location, as the photons travel further along their spiraling trajectory. Further, this representation provides a concise demonstration of the effect the energy shift has on the photons. In the presentation of the photon flux on the disk, that is Fig. 4.9 (a), the hot spot is quite clearly visible at a radius of $r \approx 5\ r_{\mathrm{g}}$. A similar photon flux is however also visible at the innermost edges of the accretion disk, where the enhanced flux in this region comes entirely from the effect of light bending. Once the energy shift is factored in, the intensity on the inner edge of the accretion disk completely overshadows the hotspot, despite their similar flux in photons. The photons incident on the inner edge of the disk were shifted to much higher energies, whereas the photons incident close to the location of emission barely received any energy shifting. One can imagine that the photons incident on the inner edge 'fell into the gravitational well' of the black hole and thereby converted their 'potential energy into kinetic energy', whereas the photons incident close to the

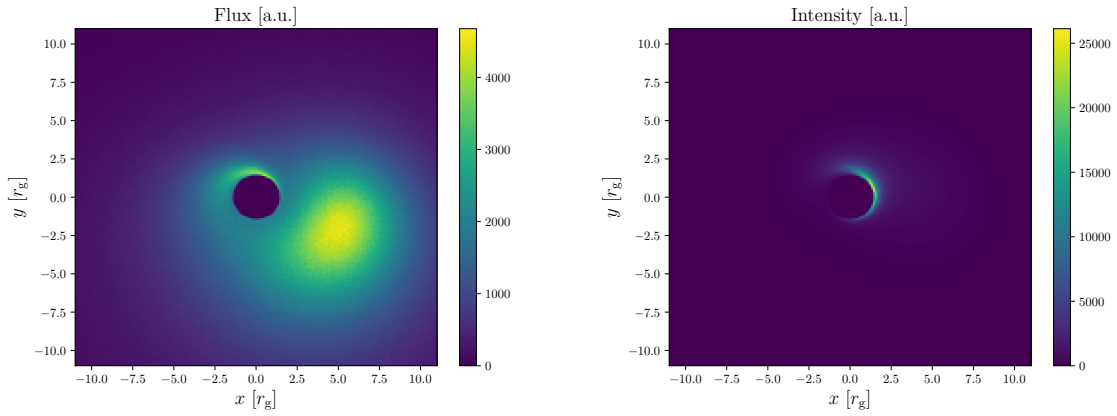


(a) (b)

**Figure 4.9:** Illumination of the accretion disk by a point source at height $h = 5\ r_g$ and located at $x = 5\ r_g$ and $y = 0\ r_g$. The figures display (a) a map of the incident flux and (b) a map of the incident intensity on the accretion disk in Cartesian coordinates $x$ and $y$. The spin parameter of the black hole was chosen as $a = 0.99$ and the source is co-rotating with the accretion disk element at $r = 5\ r_g$, in this case that is in a clockwise direction. Comparing (a) and (b) shows the relativistic effects the photons undergo along their trajectory. The intensity that is incident on the innermost radii of the disk is enhanced due to the energy shift and consequently overshadows the incident intensity on the rest of the disk.

location of emission stayed around the same equipotential line and did thus not 'gain further kinetic energy'. Note that the color scale was chosen linearly, as opposed to the logarithmic scales for flux and intensity chosen so far and also in the following simply for demonstrational purposes as the mentioned effects are best shown with this choice.

As the spacetime around a Kerr black hole is axisymmetric, a point source that strays from the rotational axis is likely to have its origin outside the black hole system itself. If the source is believed to be generated by the black hole system itself, the axisymmetry of Kerr spacetime strongly motivates an axisymmetric primary source. The simplest such source that does not trivially coincide with the lamp post case is a ring source with height $h$ and distance $x$ from the axis of symmetry. Such a ring source can be modeled as a continuum of point sources at the respective height and distance and varying $\phi$ coordinates. Due to the symmetry of Kerr spacetime, each of these point sources generates the same flux and intensity on the disk, only shifted in $\phi$ coordinate. As such it suffices to simulate a single point source and project the resulting flux and intensity onto the radius coordinate only. The flux and intensity of a ring source can therefore also be regarded as the projection of the respective spectrum of a point source onto the radial coordinate. This treatment was also used in former works on off axis sources such as Wilkins & Fabian (2012) and ensures comparability of the results.

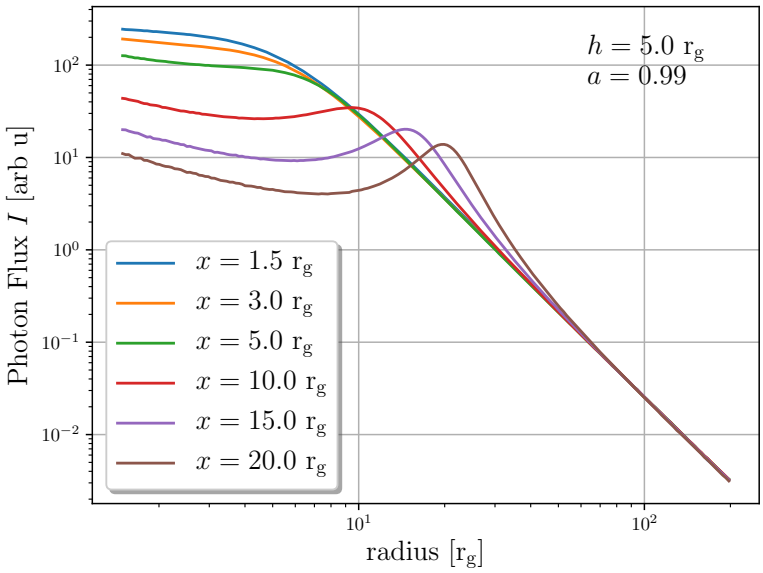


**Figure 4.10:** Photon flux profile for different source distances to the axis of symmetry. The ring source is located at a height $h = 5$ r$_g$ and the black hole has a spin parameter of $a = 0.99$. For source far away from the axis, an increase in photon counts in the region, where $r \approx x$ can be seen. The increase is expected, as the source is located directly above the corresponding disk segment.

The photon flux for a ring source is calculated according to Eq. 4.9 and is depicted in Fig. 4.11 for different emission heights and a distance to the axis of symmetry of $4\,r_g$. Figure 4.10 for an emission height $h = 5\,r_g$ and varying distances to the axis of symmetry. A depiction of the profile for varying spin parameter $a$ was deliberately omitted, as similarly to the lamp post case, it only had minor effect on the spectra. The resulting intensity profiles are depicted in Fig. 4.12 for varying emission height and in Fig. 4.13 for varying distances to the axis of symmetry.
For source heights $h \gg x$, the spectra are hardly distinguishable from the results for the lamp post geometry. This is expected, as for large source heights, a small deviation in the distance to the black hole can be regarded as negligible. At large radii $r \gg x$, the intensity profile tends again towards the $r^{-3}$ power law as expected in flat spacetime. A significant difference to the lamp post geometry can only be seen for a parameter combination where $h \leq x$. For such combinations the profiles follow a similar trend as in the lamp post case, with an additional increase of intensity and flux at $r \approx x$. This increase is explained by the enhanced photon flux close to the source location. The effect is further enhanced for increasing distance to the axis of rotation, as can be seen in Fig. 4.13. If the source is close to the black hole, i.e. for low $x$, the peak that arises at $r \approx x$ is broadened due to gravitational effects. This explains why the peaks seem to increase for increasing distance $x$ to the axis of symmetry.

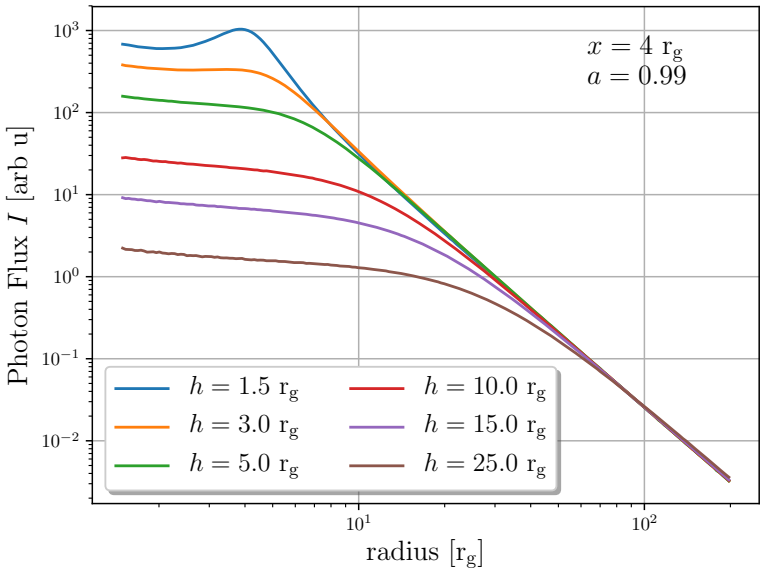


**Figure 4.11:** Photon flux profile for different primary source heights $h$. The ring source's distance to the axis of symmetry is $x = 4$ r$_g$ and the black hole spin parameter has a value of $a = 0.99$. Especially for a low source height, the increase of photon flux in the region $r \approx x$ is noticeable. The spectra of source heights much bigger than $x$ show little difference to the lamp post case (i.e. $x = 0$).

These results can again be expressed in terms of the emissivity index $\epsilon$ as already done in the lamp post case. The emissivity index for different values of emission height $h$ can be seen in Fig. 4.15 and for varying distances to the axis of symmetry in Fig. 4.14. The increase in intensity at $r \approx x$ is represented in the emissivity index by first dropping, then steepening at around this region. The steepening of the emissivity index at the innermost radii is still seen almost independently of the combination of $x$ and $h$.

For a quantitative assessment of the developed model in the case of an off-axis primary source, reference was extracted from the pdf-file of Fig.7 and Fig.13 in Wilkins & Fabian (2012). The results are compared in Fig. 4.16. For clarity's sake, the results for $x = 25$-,5-,1.235-, and 0 $r_g$ are depicted separately in Fig. 4.17. Both figures show, that the qualitative behaviour of the presented results matches that of results from previous works. However, some significant deviations are discernible. For large $x$, the peak, that arises due to the enhanced photon flux in the proximity of the source is does not coincide with the peak in the reference data. At large distances, gravitational effects are expected to become negligible. That is, in the case of $x = 25$ $r_g$, the gravitational effect on photons, that are not emitted towards the black hole, are negligible and the 'peak', that is visible is expected to be 'directly beneath' the photon source, that is, the $r$-coordinate of the center of the peak is expected to be at $r = x = 25$ $r_g$. As depicted in Fig. 4.17, in the case of $x = 25$ $r_g$, the peak has its maximum hat around $r = 24.93$ $r_g$, whereas the

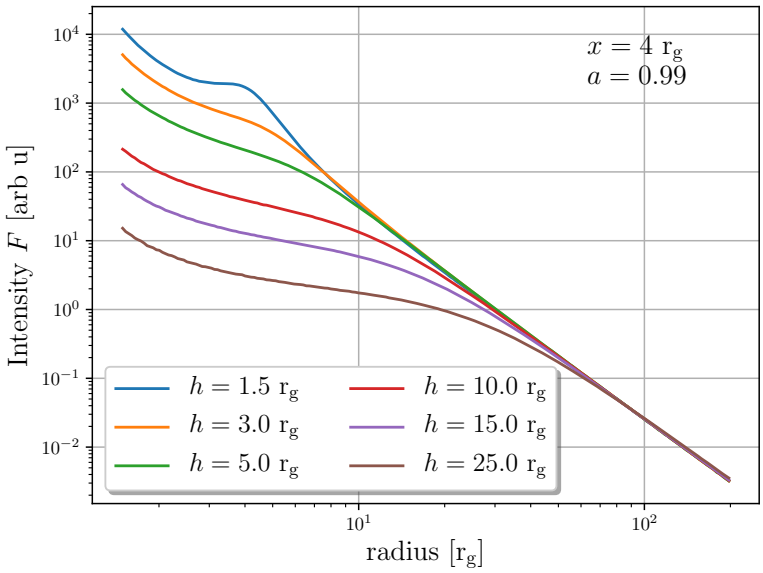


**Figure 4.12:** Intensity profile of a primary ring source at different heights with distance to the rotational axis $x = 4$ r$_g$ and a black hole spin parameter of $a = 0.99$. Again, for low source heights, the peak due to the source location can be clearly seen, whereas for large heights the effect of the source's distance to the rotational axis becomes negligible.

reference data has it's peak maximum at around $r = 22.91\ r_g$, significantly closer to the axis of symmetry than the photon source. A second peculiarity arises when inspecting the transition from off-axis sources close to the axis of symmetry to the lamp post case. Whereas for small distances to the axis of symmetry the predicted intensity at small radii is always well above the reference data, this relation is suddenly inverted when regarding the lamp post case. If assumed that the intensity profile varies smoothly with the distance to the rotational axis, such an abrupt change in behaviour is not expected. The intensity predicted by the model developed in this thesis matches very well with the assumption of smoothness when transitioning form off-axis to lamp post geometry, whereas the reference data exhibits a sudden change in behaviour under this transition. Although no definite conclusions about the validity of the developed model can be made from the comparison to the reference data, it does show, that the qualitative behaviour does match to previous work. On a quantitative level, the developed model matched the expectations even better than the reference data did.

The results presented in this chapter (with the exception of Fig. 4.9 and associated discussion) were presented under the premise of a ring source, comprised of a continuum of isotropically emitting point sources. This geometry was preferred over a point source as the axisymmetry of Kerr-spacetime strongly motivates an axisymmetric primary source. However, as discussed at the beginning of this section, these results are equivalent to the results for an isotropically emitting point source at the respective height and distance to

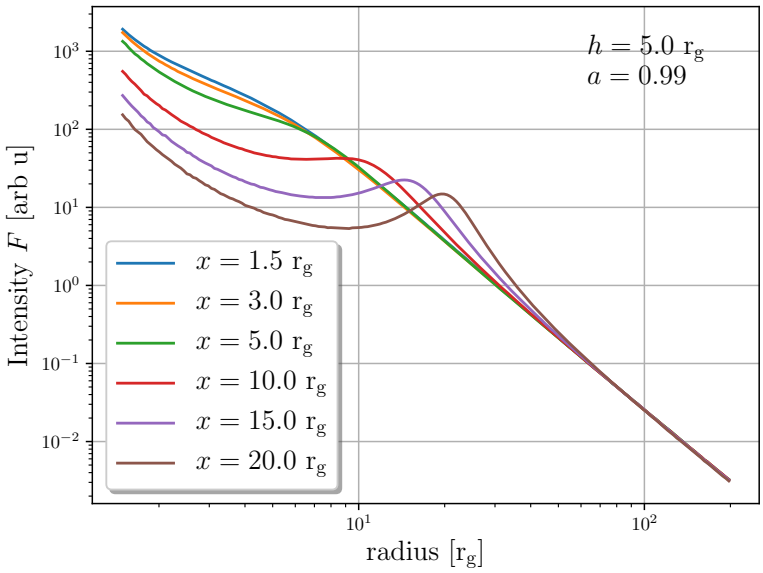


**Figure 4.13:** Intensity profile of a primary ring source at height $h = 5\ r_g$ above the black hole for varying distances $x$ to the rotational axis. The black hole spin parameter has a value of $a = 0.99$. Similarly to the photon flux, the intensity profile shows an increase at $r \approx x$, where this increase becomes more significant for sources above the outer regions of the accretion disk.

the rotational axis, if the profiles for the point source are averaged over the $\phi$-coordinate. Moreover, the presented model does not require the primary source geometry to have any symmetry whatsoever and can also calculate the $\phi$-dependence of the resulting profiles as depicted in Fig. 4.9. The assumption of an isotropically emitting source was also chosen not due to restrictions of the model, but due to the lack of reasons for assuming directional emission and for the sake of comparability to previous work.

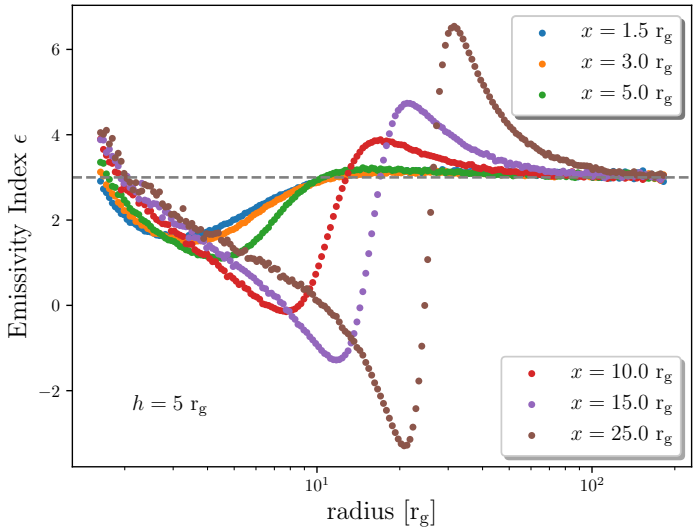


**Figure 4.14:** Emissivity index calculated from the intensity profile of a ring source at height $h = 5\ r_g$ for varying distances to the axis of symmetry and a spin parameter of $a = 0.99$. The increase in intensity at $r \approx x$ is reflected in the steepening of the emissivity index $\epsilon$ in this region. Furthermore, it appears that the further out the source is, the larger the steepening becomes.

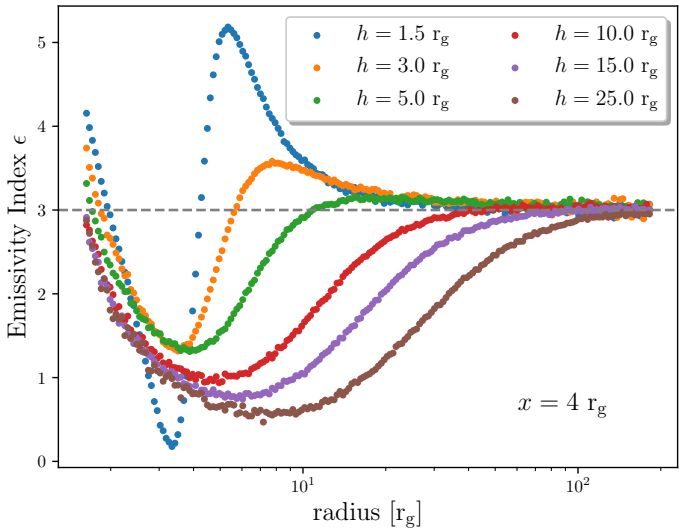


**Figure 4.15:** Emissivity index calculated from the intensity profile of a source at distance $x = 4$ r$_g$ from the rotational axis and different emission heights. The black hole spin parameter is $a = 0.99$. Again, the increase in photon flux at $r \approx x$ is reflected by a steepening of the emissivity index and it appears that this steepening is enhanced if the source is at low emission heights (and thus close to the black hole). For sources at greater heights, the steepening at the central parts of the accretion disk becomes negligible.

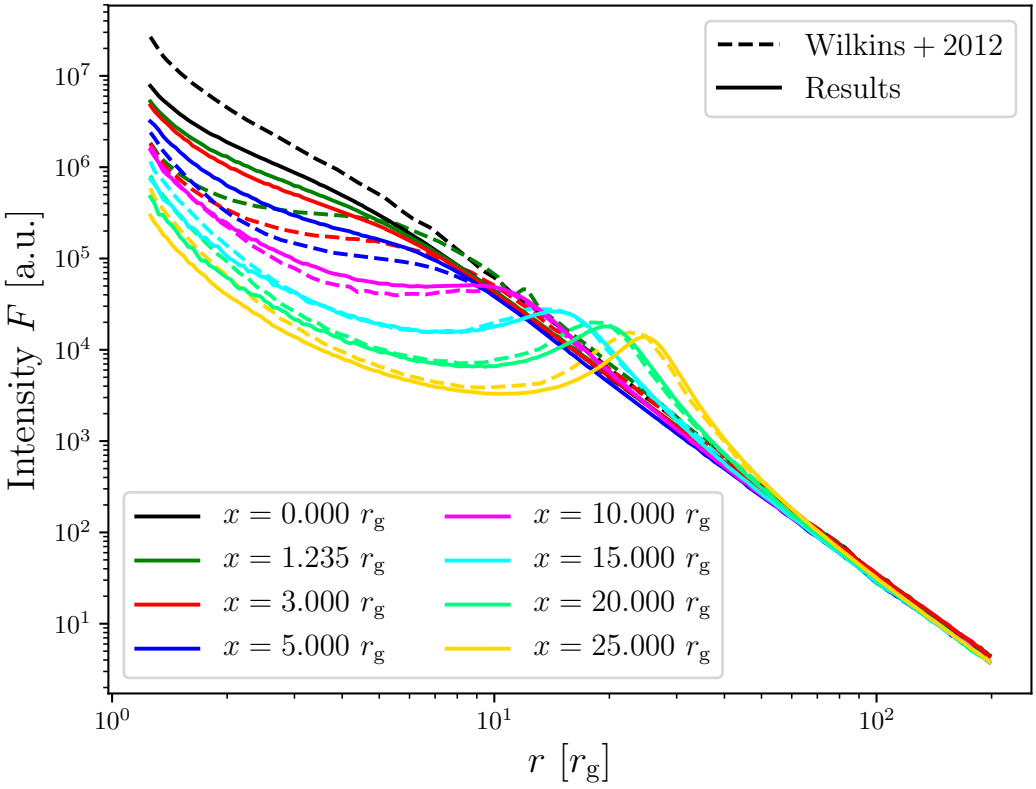


**Figure 4.16:** Comparison of the results for isotropically emitting, co-rotating ring source at height $h = 5\ r_g$ and varying distances to the axis of symmetry. Solid lines represent the results of the model developed in this thesis, while dashed lines represent the results taken from Wilkins & Fabian (2012). The lamp post case $x = 0\ r_g$ was included for the sake of comparability.

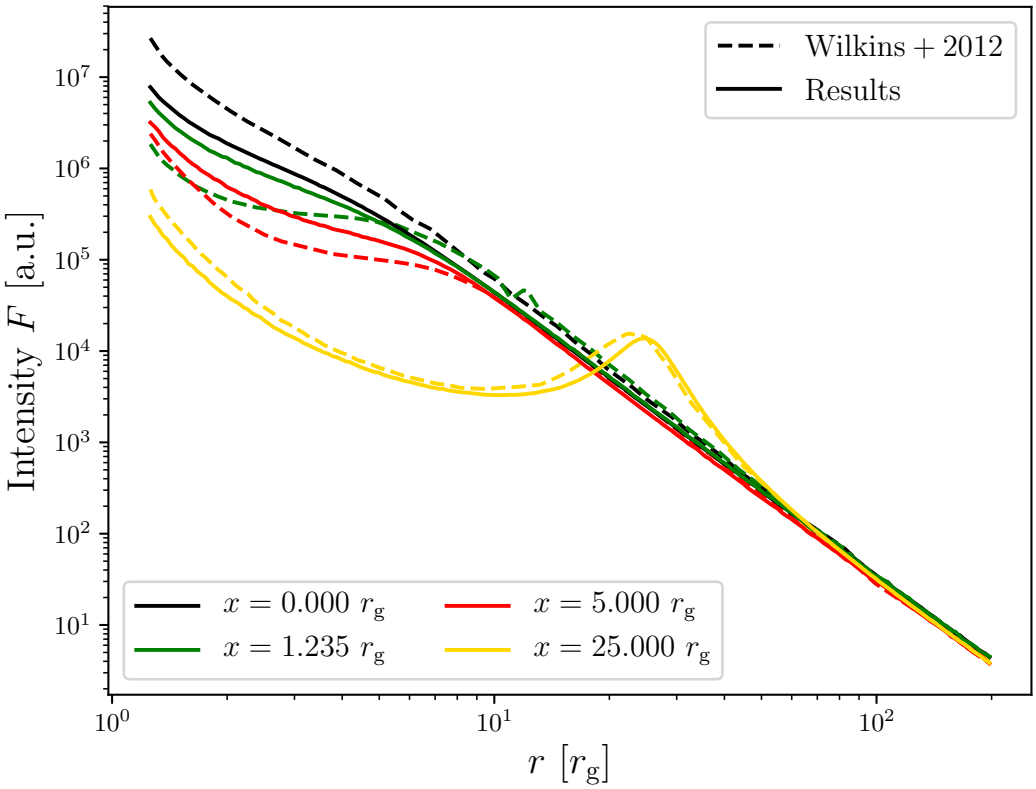


**Figure 4.17:** Comparison of the results for isotropically emitting, co-rotating ring sources at height $h = 5\ r_g$ and varying distances $x$ to the axis of symmetry to the results presented by Wilkins & Fabian (2012). In order to keep the figure clear, only $x = 0\ r_g$, $x = 1.235\ r_g$, $x = 5\ r_g$ and $x = 25\ r_g$ are depicted.

# 5. Conclusion and Future Research

In summary, this thesis has shown a fruitful approach to improve the modeling and the interpretation of relativistic reflection features. By expanding the set of possible primary source geometries in existing fitting models from the lamp post geometry to arbitrary sources of compact topology, it is possible to describe the irradiation of the accretion disk by an actual primary source instead of an empirical emissivity profile while simultaneously providing a quantitative measure on the conformity of the respective geometry to observations. The model has been compared to previous models, specifically the lamp post fitting model relxill v1.3.3 (García et al. 2014) and the results for a general point source provided by Wilkins & Fabian (2012). The here obtained results are in agreement to both of those previous models. The presented model is therefore suitable for analyzing relativistic reflection of modern and future X-ray data.

## 5.1. Alternative Accretion Disk Models

The Accretion Disk geometry assumed in this thesis is a Shakura-Sunyaev-Disk (see Shakura & Sunyaev 1973), that is an accretion disk that lies completely in the equatorial plane of the black hole. Similarly to the source in the lamp post geometry, such a disk can be at most 3-dimensional, which is unphysical. As such, the model can merely be an approximation of the real disk geometry. Indeed it would be expected that the material converges towards the equatorial plane only at small radii, whereas further out, the disk material is distributed within a certain scale height $h$ above the equatorial plane. Further, theoretical calculations involving small magnetic fields within the disk material show, that also at the innermost radii, the accretion disk is 'puffed up', indicating that even at the most crucial region for relativistic reflection, the standard model is not accurate.

Currently, models for relativistic reflection either only consider standard thin disks or if they allow for other disk geometries, they only consider specific source geometries. To date, there is no code that allows for the general modeling of both the source and the disk geometry. The code developed in this thesis thus far is only applicable to the standard disk model, however it has the potential to model other disk emissivities as well. Instead of using the *pemdisk*-function of the *YNOGK*-code provided by Yang & Wang (2013), the generalization would be based of the more general *pemfind*-function. Whereas *pemdisk* searches for the roots of the equation $\theta(p) - a = 0$, for a constant a (for the disk in equatorial plane: a=0), *pemfind* takes any algebraic equation of the coordinates $(t, r, \theta, \phi)$ and searches for roots of this equation. This generalization was not implemented yet mainly for two reasons;
Firstly *pemfind* searches for the root of an equation with 4 variables, whereas *pemdisk* generically only takes equations of one variable. As such, *pemdisk* is much faster and thus more fitting for the task of creating a table model for the thin disk geometry.
Secondly, tests on the *pemfind* function showed that not all photon trajectories that are incident on the disk were marked as such by the *pemfind* function. Further, some trajectories were assigned negative values for the photon trajectory parameter $p$ as the

result of the *pemfind*-function. However, as defined in eq. 3.15, $p$ is a positive real meaning that the code did not operate as expected. Fortunately, this does not seem to be a principal problem with the way the code operates but rather an issue of bug fixing. The geometry of the disk (as long as it can be expressed in terms of an algebraic equation or finite compositions thereof) can potentially be considered by the presented code as well and subsequently included into the model.

## 5.2. Physical Modeling of the Primary X-ray Source

Expanding on the already existing models for lamp post sources, a method for the modeling of the illumination of the accretion disk by a general photon source based on physical parameters of the source geometry was developed in this thesis. Contrary to current practice, the presented approach allows to model the actual geometry of the irradiating source instead of assuming a composition of power laws for fit routines. This helps extract information about the location and shape of the primary source.

Although the lamp post model describes many of the observed phenomena, it assumes a source with no width along the axis of symmetry. Such a source would be at most 2 dimensional, which is in stark contrast to the 4 dimensional paradigm of general relativity as well as common intuition. The primary source is therefore suspected to be of finite extension with the lamp post only being an approximation of a compact source on the rotational axis.
Through the process of fitting the developed model to observational data, the extension of the source may be inferred. As an example, in the work of Wilkins & Fabian (2012), observational data on the narrow Line Seyfert galaxy 1H 0707−495 was compared to results of their own model, see Fig. 5.1. The emissivity profile of 1H 0707−495 was determined in Wilkins & Fabian (2011) by fitting for the relative contribution of the relativistically blurred K emission line components from successive annuli in the accretion disk. They then determined suitable parameters for the height and distance to the axis of symmetry of emitting point sources such that the sum of their contributions would resemble the observed profile. From this, they concluded that a significant portion of the photons must originate from a source closer than 2 $r_{\mathrm{g}}$ to the reflector.
In a similar fashion, Wilkins et al. (2015) investigated the emissivity profile of Mrk 335. The observed data can be found in Fig. 5.2. From this data, they determined an upper limit to the source extent of about 5 $r_{\mathrm{g}}$. Both of these analyses provide valuable insight on the geometry of the primary X-ray source.
Due to the long runtime of the simulations used to determine the theoretical emissivity profile for different geometries, these parameters however could not be fit to the observed data. The code developed in this thesis proves to be sufficiently fast to calculate and subsequently tabulate emissivity profiles for varying source heights and distances to the rotational axis. The tabulated data for point sources can then be added to construct extended sources. In this way a table model for general photon sources in the vicinity of a Kerr black hole arises, which can be used to fit to observational data. From this, physical parameters for the geometry of the corona can directly be extracted from the fit

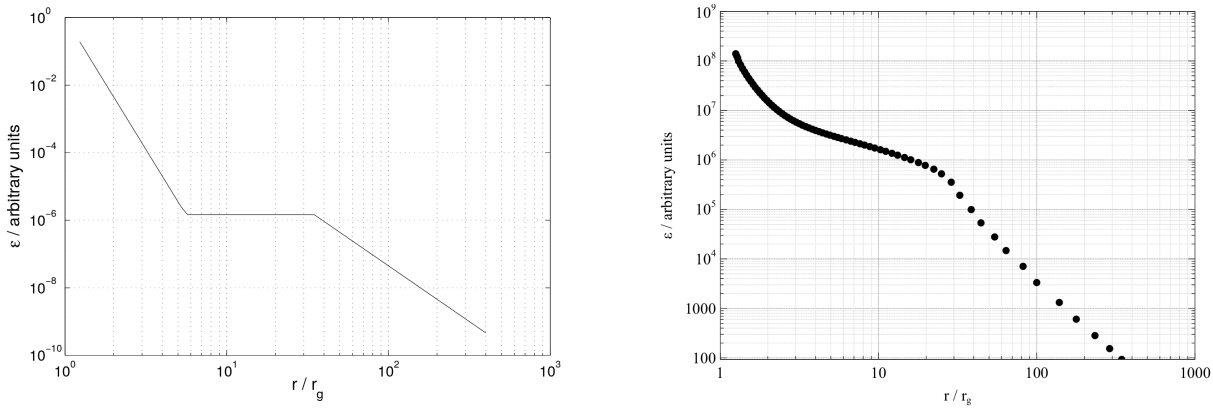


**Figure 5.1:** (a) Emissivity profile determined for X-ray reflection from the accretion disk in 1H 0707-495 in January 2008 by fitting for the relative contributions of components of the relativistically broadened iron K emission line from successive radii in the disk, compared with (b), a theoretical emissivity profile due to a radially extended X-ray source between 2 and 10 $r_{\rm g}$ above the disk plane and extending radially to about 30 $r_{\rm g}$. Figures taken from Wilkins & Fabian (2012).

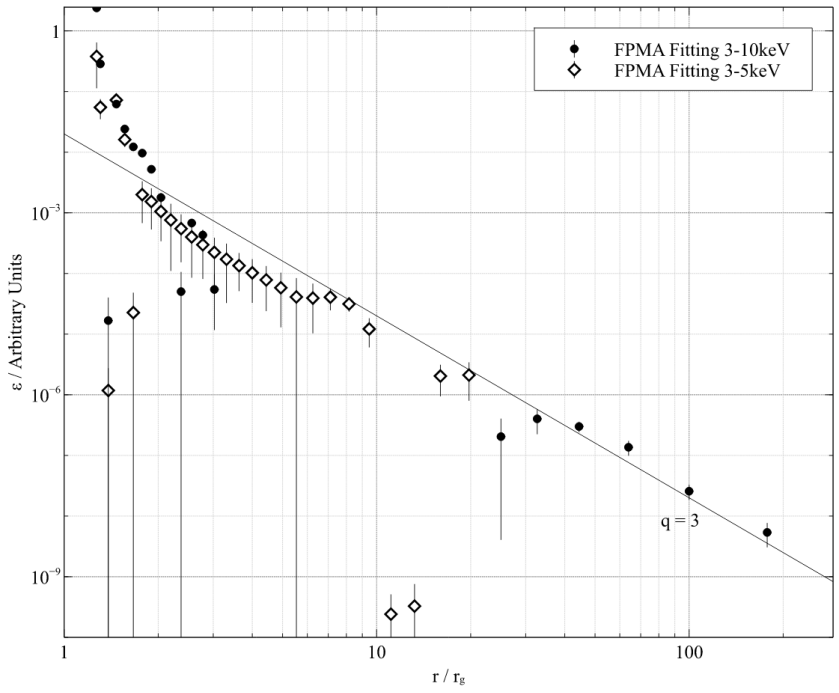


**Figure 5.2:** Emissivity profile of the accretion disk of Mrk 335 on the decline of the X-ray flare in 2014 measured by the *NuSTAR* FPMA spectrum. The profile is determined by fitting for the contributions of successive annuli in the accretion disk to the components of the relativistically broadened iron K emission line. Additionally the case of a single power law $\propto r^{-3}$ is added for comparability. Figure taken from Wilkins et al. (2015).

of the model to measured data.
The here developed model however is capable of additionally providing quantitative statements on the conformity of the geometry to the data by means of fitting the results to the observed emissivity profiles.

## 5.3. Modeling of the Relativistic Reflection

Inferring the emissivity profile from the observed energy spectrum yields rather crude data, as can be seen in Fig. 5.1 (a). A more self-consistent approach would be to model the complete observed spectrum and fit the source geometry to this data instead of the inferred emissivity profile. This can be done by providing updated emissivity profiles for arbitrary source geometries by means of the here developed method to codes such as the *relxill* model (see Dauser et al. 2013; García et al. 2014), which calculate the reflection on the accretion disk and the relativistic effects occurring on the way from the reemission on the disk to the observer. Expanding the *relxill* model in this fashion, one can simulate the relativistically broadened reflection spectrum seen from the accretion disk for arbitrary source geometries. The broadened K$\alpha$ lines for the lamp post geometry were already calculated before e.g. by Dauser et al. (2013) and are displayed in Fig. 5.3, showing the effect of relativistic smearing on a $\delta$-distribution like emission. Similarly to the lamp post case, the reflection spectrum for the case of an arbitrary X-ray source can be calculated by using the irradiated spectrum on the accretion disk and calculating the fluorescent emission through involved radiative transfer calculations and taking into account the fluorescent yield of the various components. The *relxill* model then determines the emissivity of the accretion disk based on the incident spectrum and can thus simulate the observed emission spectrum. Note that in the *relxill* model, the emissivity of the disk is not only a fitting parameter, but depends on the incident spectrum, which directly establishes a connection to the primary source geometry. This treatment allows for direct comparison of the observed reflection spectrum and the simulation based on the irradiating source's geometry.

Additionally to the investigation of the reflection features, information from photons that reach the observer directly can be used as well. Photons emitted by the primary source may be reflected on the accretion disk and then reach the observer after reflection or they can reach the observer on a direct path, i.e. without prior reflection on the disk. These two types of photons are expected to have different energies, with the photons that reach the observer directly being in the hard X-ray band and the reflected photons being in the soft X-ray band of the spectrum. Therefore these two types of photons can be distinguished in the observed spectrum. Further, depending on the primary source's location and geometry, the photons that are reflected on the disk before being observed generally travel 'further' than photons that reach the observer directly. This difference in path length directly translates into a difference in arrival time of the photons at the observer. In the vicinity of a black hole of mass $M = 2 \cdot 10^6 M_\odot$, photons need about 9.8 s to travel a distance of 1 $r_\mathrm{g}$ (Emmanoulopoulos et al. 2014). Variations in the soft band of the spectrum are thus expected to noticeably lag behind variations in the hard

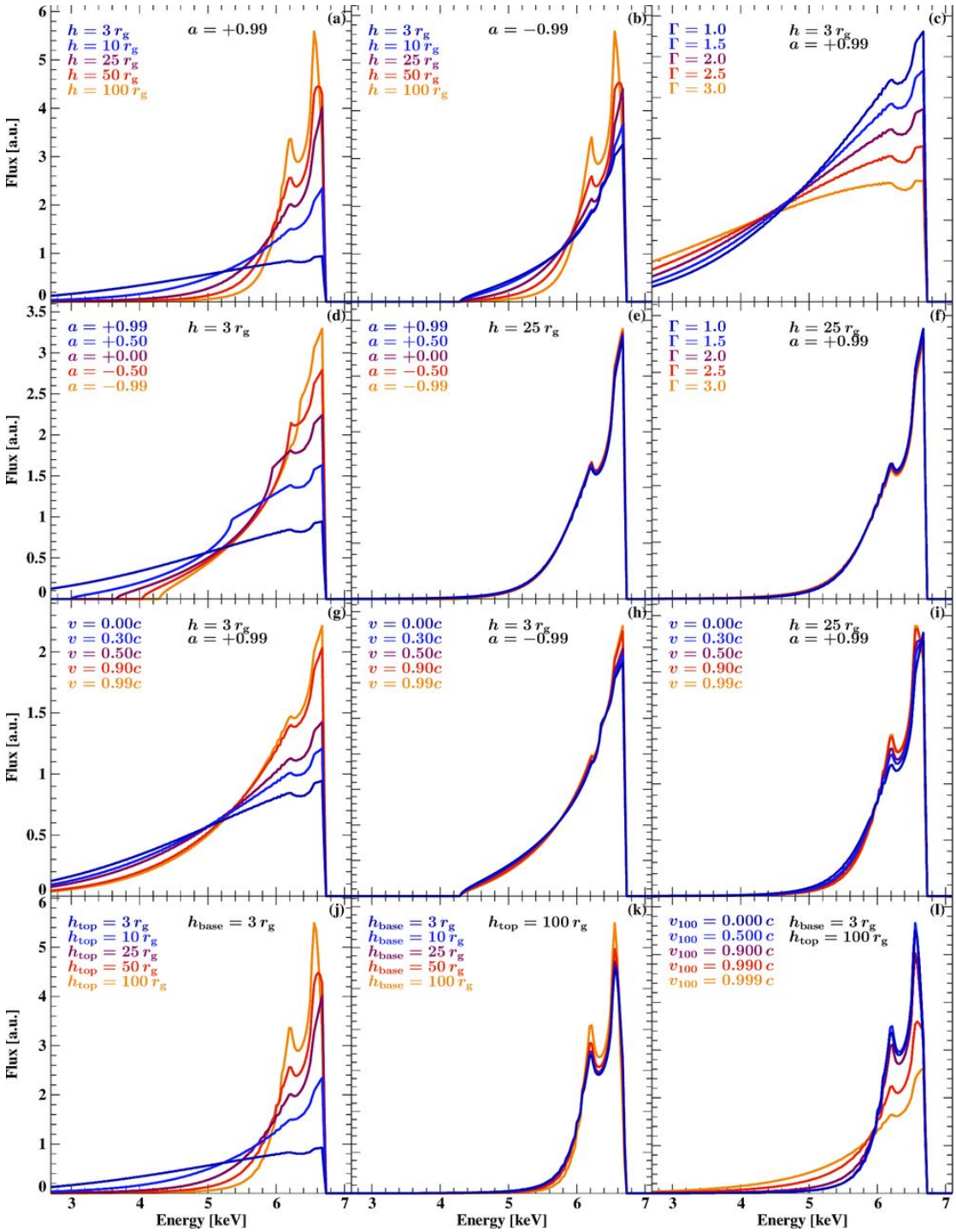


**Figure 5.3:** Line profiles of the RELLINE$_{\rm LP}$ model for different parameters. If not stated differently $a = 0.99$ and $h = 3\ r_{\rm g}$ is assumed. The inclination is fixed at i = 30° and the outer edge of the disc at $r_{\rm out} = 400\ r_{\rm g}$. Note that we always assume that the inner edge of the accretion disc coincides with the ISCO. All profiles are normalized to have equal area, i.e. the number of photons producing each reflection feature is equal. Figure taken from Dauser et al. (2013).

band of the observed spectrum due to difference in path length of directly observed and reflected photons. Information about the height of the primary source above the accretion disk is therefore encoded in these time lags. For the case of the lamp post geometry, Emmanoulopoulos et al. (2014) presented an approach to systematically investigated the time lags and infer the height of the emitting source. The method for tracing photons in Kerr-spacetime presented in this thesis can be used to generalize their approach as to also include compact sources of arbitrary geometry. Again, this treatment allows for extraction of physical properties of the primary source by comparison of data from timed observations with the simulation.

# A. On the derivation of the Kerr metric

For clarity's sake, the proof of the claimed diagonizability of the metric tensor with respect to the two coordinates $\tilde{x}^2$ and $\tilde{x}^3$ (Eq. 2.2) is presented in the appendix rather than the main part of the thesis. For a more in-depth explanation of this proof and on the derivation of the Kerr metric in general, the reader is referred to Chandrasekhar (1983).

In section 2.1 it was claimed that the expression

$$\mathrm{d}s^2 = g_{11}(\mathrm{d}x^1)^2 + 2g_{12}(\mathrm{d}x^1\mathrm{d}x^2) + g_{22}(\mathrm{d}x^2)^2 \tag{A.1}$$

can be brought to the form

$$(\mathrm{d}s')^2 = g_{1'1'}(\mathrm{d}x^{1'})^2 + g_{2'2'}(\mathrm{d}x^{2'})^2 \tag{A.2}$$

by a coordinate transformation. Indeed we will now show (following Chandrasekhar 1983), that the presented line element (with assumed signature (2,0) or (0,2), i.e. (+,+) or (-,-), as $x^1$ and $x^2$ are both spatial coordinates) can be brought to the form in Eq. (A.2), even further, in this form it is achievable that $g_{1'1'} = g_{2'2'}$. For a coordinate transformation $x^{1'} = \varphi(x^1, x^2), x^{2'} = \psi(x^1, x^2)$ to reduce the contravariant form of the metric

$$\mathrm{d}s^2 = g^{11}(\mathrm{d}x_1)^2 + 2g^{12}(\mathrm{d}x_1\mathrm{d}x_2) + g^{22}(\mathrm{d}x_2)^2 \tag{A.3}$$

to a diagonal from with equal coefficients for $(\mathrm{d}x_1)^2$ and $(\mathrm{d}x_2)^2$, it is both necessary and sufficient, that

$$g^{1'2'} = g^{ab}\frac{\partial x_{1'}}{\partial x_a}\frac{\partial x_{2'}}{\partial x_b} = 0 \qquad a, b = 1, 2 \tag{A.4}$$

which is the condition to make the resulting metric diagonal, and

$$g^{1'1'} - g^{2'2'} = g^{ab}\left(\frac{\partial x_{1'}}{\partial x_a}\frac{\partial x_{1'}}{\partial x_b} - \frac{\partial x_{2'}}{\partial x_a}\frac{\partial x_{2'}}{\partial x_b}\right) = 0 \qquad a, b = 1, 2 \tag{A.5}$$

which is the condition that the coefficients be equal. Condition (A.4) is fulfilled by any transformation ($\varphi$, $\psi$) of the kind

$$\begin{aligned}
\frac{\partial\varphi(x_1, x_2)}{\partial x_1} &= \kappa\left(g^{21}\frac{\partial\psi(x_1, x_2)}{\partial x_1} + g^{22}\frac{\partial\psi(x_1, x_2)}{\partial x_2}\right) = \kappa g^{2k}\frac{\partial\psi(x_1, x_2)}{\partial x_k} \qquad k = 1, 2 \\
\frac{\partial\varphi(x_1, x_2)}{\partial x_2} &= -\kappa\left(g^{11}\frac{\partial\psi(x_1, x_2)}{\partial x_1} + g^{12}\frac{\partial\psi(x_1, x_2)}{\partial x_2}\right) = -\kappa g^{1k}\frac{\partial\psi(x_1, x_2)}{x_k} \qquad k = 1, 2.
\end{aligned} \tag{A.6}$$

Substituting this into Eq. (A.5) yields the condition

$$\left(\kappa^2\{g^{11}g^{22} - (g^{12})^2\} - 1\right)\left[g^{11}(\psi_{,1})^2 + 2g^{12}\psi_{,1}\psi_{,2} + g^{22}(\psi_{,2})^2\right], \tag{A.7}$$

where the $_{,k}$ denotes the derivative with respect to the $k$-th coordinate. For a metric with positive or negative definite signature, the expression in square brackets in Eq. (A.7) cannot vanish, thus the condition is only and always fulfilled for

$$\kappa^2 = \frac{1}{g^{11}g^{22} - (g_{12})^2} = g_{11}g_{22} - (g_{12})^2 = \det(g_{ab}). \tag{A.8}$$

Thus in combination with Eq. A.4, the transformation

$$\varphi_{,1} = \sqrt{\det(g_{ab})}g^{2k}\psi_{,k} \tag{A.9}$$

$$\varphi_{,2} = \sqrt{\det(g_{ab})}g^{1k}\psi_{,k} \qquad k = 1, 2. \tag{A.10}$$

The integrability condition then becomes

$$\left(\sqrt{\det(g_{ab})}g^{ik}\psi_{,k}\right)_{,i} = 0, \tag{A.11}$$

meaning that $\psi$ can be *any* solution to the Laplace equation in 2-dimensions. The existence of a solution is guaranteed by the theory of partial differential equations.

# References


Abramowitz M., Stegun I.A., 1965, Handbook of mathematical functions with formulas, graphs, and mathematical tables, Dover Publications Inc.

Balbus S.A., Hawley J.F., 1991, ApJ 376, 214

Bardeen J.M., Press W.H., Teukolsky S.A., 1972, ApJ 178, 347

Bartelmann M., 2010, Classical and Quantum Gravity 27, 233001

Blandford R.D., 1999, In: Sellwood J.A., Goodman J. (eds.) Astrophysical Discs - an EC Summer School, Vol. 160. Astronomical Society of the Pacific Conference Series, ASP, p. 265

Blandford R.D., Znajek R.L., 1977, MNRAS 179, 433

Boyer R.H., Lindquist R.W., 1967, J. Math. Phys. 8, 265

Brenneman L.W., Reynolds C.S., Nowak M.A., et al., 2011, ApJ 736, 103

Carlson B., 1988, Math. Comp 51, 276

Carlson B., 1989, Math.Comp 53, 327

Carlson B., 1991, Math.Comp 56, 267

Carlson B., 1992, Math.Comp 59, 165

Carter B., 1968, Phys. Rev. 174, 1559

Carter B., 1968, Commun. Math. Phys. 10, 280

Chandrasekhar S., 1983, The Mathematical Theory of Black Holes, Clarendon Press and Oxford Univ. Press, Oxford

Cunningham C.T., 1975, ApJ 202, 788

Dauser T., 2010, *Master's thesis*, Friedrich-Alexander University Erlangen-Nurnberg, Erlangen

Dauser T., 2014, Ph.D. thesis, Friedrich-Alexander University Erlangen-Nurnberg, Erlangen

Dauser T., Garcia J., Wilms J., et al., 2013, MNRAS 430, 1694

Dauser T., Svoboda J., Schartel N., et al., 2012, MNRAS 422, 1914

Dexter J., Agol E., 2009, ApJ 696, 1616

Emmanoulopoulos D., Papadakis I.E., Dovčiak M., McHardy I.M., 2014, MNRAS 439, 3931

Fabian A.C., Vaughan S., 2003, MNRAS 340, L28

Fabian A.C., Vaughan S., Nandra K., et al., 2002, MNRAS 335, L1

Fukumura K., Kazanas D., Stephenson G., 2009, ApJ 695, 1199

Gallo L.C., Miniutti G., Miller J.M., et al., 2011, MNRAS 411, 607

García J., Dauser T., Lohfink A., et al., 2014, ApJ 782, 76

Garofalo D., Evans D.A., Sambruna R.M., 2010, MNRAS 406, 975

Kamraj N., Rivers E., Harrison F.A., et al., 2017, ApJ 843, 89

Kerr R.P., 1963, Phys. Rev. Lett. 11, 237

Kolonko M., 2008, Stochastische Simulation, Vieweg+Teubner

Krishan V., Mahajan S.M., 2008, In: Hasan S.S., Gangadhara R.T., Krishan V. (eds.) Turbulence, Dynamos, Accretion Disks, Pulsars and Collective Plasma Processes., Springer Netherlands, Dordrecht, p.233

Krolik J.H., 1999, Active galactic nuclei : from the central black hole to the galactic environment, Princeton University Press

Ludvigsen M., 1999, General Relativity: A Geometric Approach, Cambridge University Press, Cambridge

Martocchia A., Matt G., Karas V., 2002, A&A 383, L23

Miniutti G., Fabian A.C., 2004, MNRAS 349, 1435

Miniutti G., Fabian A.C., Goyder R., Lasenby A.N., 2003, MNRAS 344, L22

Misner C.W., Thorne K.S., Wheeler J.A., 1973, Gravitation, Princeton University Press and

W. H. Freeman Co.
Murdin P., Webster B.L., 1971, Nat 233, 110
Nagaraja M.P., 2019, Black Holes, https://science.nasa.gov/astrophysics/focus-areas/black-holes Accessed: 2019-11-03
Newman E.T., Couch E., Chinnapared K., et al., 1965, J. Math. Phys. 6, 918
Novikov I.D., Thorne K.S., 1973, Astrophysics of Black Holes, http://www.its.caltech.edu/~kip/index.html/PubScans/II-48.pdf Accessed: 2019-08-30
Orito S., Yoshimura M., 1985, Phys. Rev. Lett. 54, 2457
Orosz J.A., McClintock J.E., Aufdenberg J.P., et al., 2011, ApJ 742, 84
Reynolds C.S., Nowak M.A., 2003, Phys.Rept. 377, 389
Risaliti G., Harrison F.A., Madsen K.K., et al., 2013, Nat 494, 449
Schwarzschild K., 1916, Sitzungsber. Preuss. Akad. Wiss. Berlin (Math. Phys.) 1916, 189
Shakura N.I., 1987, Soviet Astronomy Letters 13, 99
Shakura N.I., Sunyaev R.A., 1973, A&A 24, 337
Speith R., Riffert H., Ruder H., 1995, Comput. Phys. Commun. 88, 109
Sunyaev R.A., Truemper J., 1979, Nat 279, 506
Thorne K.S., 1974, ApJ 191, 507
Vaughan S., Fabian A.C., 2004, MNRAS 348, 1415
Walton D.J., Nardini E., Fabian A.C., et al., 2013, MNRAS 428, 2901
Webster B.L., Murdin P., 1972, Nat 235, 37
Wilkins D.R., Fabian A.C., 2011, MNRAS 414, 1269
Wilkins D.R., Fabian A.C., 2012, MNRAS 424, 1284
Wilkins D.R., Gallo L.C., Grupe D., et al., 2015, MNRAS 454, 4440
Wilms J., Reynolds C.S., Begelman M.C., et al., 2001, MNRAS 328, L27
Wilson A.S., Colbert E.J.M., 1995, ApJ 438, 62
Yang X., Wang J., 2013, ApJS 207, 6

# Acknowledgements

I would like to thank my advisor and supervisor Jörn Wilms for providing me with the subject of this thesis and the possibility to do my master's thesis at the Dr. Karl Remeis observatory in Bamberg. Moreover I want to thank him for always providing a fresh view on issues and for creating such a pleasant working group.

Further I owe a large 'thank you' to my second advisor Thomas Dauser for a multitude of reasons. First and foremost I want to thank him for his guidance throughout the entire thesis. It was a pleasure exchanging ideas with him and he made his groundlaying work on the topic as understandable to me as possible. Next to his aid in scientific matters, I also want to thank him for all the advice he has given to me concerning writing and structuring the thesis. Without his help, this thesis would not have been possible in the form it is today. Additionally, Thomas introduced me to a variety of interesting people, including Javier García and Riley Connors from the Divison of Physics and Mathematics at Caltech. Lastly I want to thank him for writing a very comprehensible dissertation as well as diploma thesis, allowing me to begin working in the field easily.

I also want to express my gratitude towards my office colleagues Ralf Ballhausen, Dominik Bernreuther and Katrin Berger for making me feel welcome from the very first day and making the time at the office more of a pleasure than an obligation. The conversations with you could range from purely philosophical to very work related topics and I enjoyed every one of them. Thank you for making my time at the observatory so enjoyable.

I want to separately thank Ralf Ballhausen again. For one, he helped me get used to a bunch of useful software, introduced me to working with a git repository and helped me a ton in writing and dealing with FITS files. I feel very fortunate to have had him as a reliable and helpful colleague in my office. Moreover, Ralf played a major part in organizing group activities for all the people at the observatory and making work so enjoyable. Be it the regular cake time in the observatory kitchen, the organization of a Remeis Pool for cooling during summer times or organizing the Remeis Winter Party, he was always among the main contributors.

There are few places I felt as comfortable and as welcome as at the Dr. Karl Remeis observatory, which is why I want to thank every member working there for maintaining such a pleasant and familiar atmosphere. A large 'thank you' is also directed to the the system administrators of the observatory for keeping everything running.

Lastly I deeply want to express my gratitude towards my family. To both of my parents, for always supporting me in every conceivable manner and being there for me at whatever time it is needed. Thank you very much. I also want to thank my brother for his advice on many situations in life and for always offering his help, no matter the issue at hand. I am very fortunate to have all of you.

# Declaration

Hiermit versichere Ich, Stefan Lickleder, dass ich die vorliegende Arbeit ohne fremde Hilfe und ohne Benutzung anderer als der angegebenen Quellen angefertigt habe. Alle Ausführungen, die wörtlich oder sinngemäß übernommen wurden, sind als solche gekennzeichnet.
Die Arbeit hat in gleicher oder ähnlicher Form noch keiner anderen Prüfungsbehörde vorgelegen.

Ort, Datum

Lickleder Stefan